6-21-2017

Ca2+-permeable AMPARs mediate glutamatergic transmission and excitotoxic damage at the hair cell ribbon synapse

Joy Y. Sebe
University of Washington, Seattle

Soyoun Cho
University of Washington, Seattle

Lavinia Sheets
Harvard Medical School

Mark A. Rutherford
Washington University School of Medicine in St. Louis

Henrique von Gersdorff
Oregon Health & Science University

See next page for additional authors

Cellular/Molecular

Ca^{2+}-Permeable AMPARs Mediate Glutamatergic Transmission and Excitotoxic Damage at the Hair Cell Ribbon Synapse

Joy Y. Sebe,[1] Soyoun Cho,[2] Lavinia Sheets,[3] Mark A. Rutherford,[4] Henrique von Gersdorff,[5] and David W. Raible[1]

[1]Departments of Biology and Biological Structure, University of Washington, Seattle, Washington 98195-7420, [2]Center for Sensory Neuroscience, Boys Town National Research Hospital, Omaha, Nebraska 68131, [3]Eaton-Peabody Laboratories, Massachusetts Eye and Ear, Department of Otolaryngology, Harvard Medical School, Boston, Massachusetts 02114, [4]Department of Otolaryngology, Washington University in St. Louis, St. Louis, Missouri 63110, and [5]The Vollum Institute, Oregon Health & Science University, Portland, Oregon 97239

We report functional and structural evidence for GluA2-lacking Ca^{2+}-permeable AMPARs (CP-AMPARs) at the mature hair cell ribbon synapse. By using the methodological advantages of three species (of either sex), we demonstrate that CP-AMPARs are present at the hair cell synapse in an evolutionarily conserved manner. Via a combination of *in vivo* electrophysiological and Ca^{2+} imaging approaches in the larval zebrafish, we show that hair cell stimulation leads to robust Ca^{2+} influx into afferent terminals. Prolonged application of AMPA caused loss of afferent terminal responsiveness, whereas blocking CP-AMPARs protects terminals from excitotoxic swelling. Immunohistochemical analysis of AMPAR subunits in mature rat cochlea show regions within synapses lacking the GluA2 subunit. Paired recordings from adult bullfrog auditory synapses demonstrate that CP-AMPARs mediate a major component of glutamatergic transmission. Together, our results support the importance of CP-AMPARs in mediating transmission at the hair cell ribbon synapse. Further, excess Ca^{2+} entry via CP-AMPARs may underlie afferent terminal damage following excitotoxic challenge, suggesting that limiting Ca^{2+} levels in the afferent terminal may protect against cochlear synaptopathy associated with hearing loss.

Key words: cochlear synaptopathy; excitotoxicity; GCaMP; noise overexposure; zebrafish

Significance Statement

A single incidence of noise overexposure causes damage at the hair cell synapse that later leads to neurodegeneration and exacerbates age-related hearing loss. A first step toward understanding cochlear neurodegeneration is to identify the cause of initial excitotoxic damage to the postsynaptic neuron. Using a combination of immunohistochemical, electrophysiological, and Ca^{2+} imaging approaches in evolutionarily divergent species, we demonstrate that Ca^{2+}-permeable AMPARs (CP-AMPARs) mediate glutamatergic transmission at the adult auditory hair cell synapse. Overexcitation of the terminal causes Ca^{2+} accumulation and swelling that can be prevented by blocking CP-AMPARs. We demonstrate that CP-AMPARs mediate transmission at this first-order sensory synapse and that limiting Ca^{2+} accumulation in the terminal may protect against hearing loss.

Introduction

Long-term studies of the mammalian cochlea have recently revealed that even a single incidence of noise overexposure can produce cochlear synaptopathy and neurodegeneration, exacerbating age-related hearing loss (Kujawa and Liberman, 2009; Lin et al., 2011). A major advance toward understanding this synaptopathy is to determine the cause of the initial excitotoxic insult.

Received Nov. 23, 2016; revised April 20, 2017; accepted April 24, 2017.

Author contributions: J.Y.S., S.C., L.S., M.A.R., H.v.G., and D.W.R. designed research; J.Y.S., S.C., L.S., and M.A.R. performed research; J.Y.S., S.C., L.S., and M.A.R. analyzed data; J.Y.S., S.C., L.S., M.A.R., H.v.G., and D.W.R. wrote the paper.

This work was supported by the National Institutes of Health via National Institute on Deafness and Other Communication Disorders (NIDCD) Grants R03-DC-014006 to J.Y.S., R01-DC-014712 to M.A.R., R01-DC-004274 to H.v.G., and R01-DC-005987 to D.W.R. L.S. was supported by The Amelia Peabody Charitable Fund and NIDCD Grant R01-DC-012838 to W.F. Sewell (Dept. of Otolaryngology, Harvard Medical School). M.A.R. was also supported by an International Project Grant from Action on Hearing Loss. We thank Ed Rubel for his key scientific insights regarding the work.

The authors declare no competing financial interests.

Correspondence should be addressed to either of the following: David Raible, Department of Biological Structure, University of Washington, Seattle, WA 98195-7420, E-mail: draible@uw.edu; or Joy Sebe, Department of Biology, University of Washington, Seattle, WA 98195-7420, E-mail: sebe@uw.edu.

DOI:10.1523/JNEUROSCI.3644-16.2017

 0270-6474/17/376162-14$15.00/0

This requires a more comprehensive understanding of the glutamate receptors that mediate synaptic function.

Much of our knowledge regarding the hair cell afferent synapse has been acquired from experiments performed in explanted endorgans of the prehearing animal (Glowatzki and Fuchs, 2002; Goutman and Glowatzki, 2007; Zhang-Hooks et al., 2016). It is widely assumed that glutamatergic transmission at this sensory synapse is mediated exclusively by Ca^{2+}-impermeable AMPA receptors that include the Ca^{2+}-limiting GluA2 subunit (Jonas and Burnashev, 1995). This assumption is supported by histological studies showing the expression of GluA2/3 and GluA4 at developing and mature cochlear hair cell synapses (Kuriyama et al., 1994; Matsubara et al., 1996; Fujikawa et al., 2014). Until now, there has been no evidence for postsynaptic regions lacking the GluA2 subunit and functional Ca^{2+}-permeable AMPA receptors (CP-AMPARs) at the adult hair cell synapse.

To examine AMPARs that mediate synaptic transmission in maturing and adult synapses, we made use of the unique advantages of the following three model systems: zebrafish, rat, and bullfrog. The zebrafish skin is lined with clusters of hair cells that are both structurally and functionally similar to hair cells of the inner ear (Trapani and Nicolson, 2011; Maeda et al., 2014). Lateral line hair cells start mechanotransducing by 3 d postfertilization (Kindt et al., 2012), and by 5 dpf larvae are already using the lateral line to navigate their environment (Suli et al., 2012; Stewart et al., 2013). Given their external location, lateral line hair cells are optimal for *in vivo* Ca^{2+}-imaging experiments and easily accessible for mechanical stimulation. Despite the methodological advantages and valuable insights gained from zebrafish (Söllner et al., 2004; Nicolson, 2005), novel findings in fish and other simple organisms are accompanied by questions regarding the relevance of new data to more complex organisms. To address this concern as well as to determine the applicability of lateral line findings to auditory organs, we performed work in both rat and frog auditory synapses. Functional studies, including Ca^{2+} imaging and electrophysiology, of the mature mammalian inner hair cell synapse are challenging given the limited access to hair cells and spiral ganglion neurons (SGNs; Chang et al., 2010; Wang et al., 2013). We thus made use of high-resolution immunohistochemical analysis of mature rat cochlear synapses to determine whether AMPAR subunit compositions that are consistent with CP-AMPARs can be observed. Last, we used the adult bullfrog preparation to determine whether CP-AMPARs mediate transmission in a bona fide auditory synapse. Each model organism provides a unique contribution to the work that addresses the caveats of the others to provide a more comprehensive story of the AMPARs present at the hair cell synapse.

In addition to examining synaptic transmission, we used zebrafish to examine the role of CP-AMPARs in excitotoxic damage of postsynaptic neurons. Calcium entry through ionotropic glutamate receptors (iGluRs), primarily via NMDA receptors (NMDARs), underlies excitotoxicity throughout the nervous system (Lau and Tymianski, 2010). In some contexts, CP-AMPARs are the critical iGluRs in this process (Liu and Zukin, 2007). In fact, the most promising evidence that CP-AMPARs may be expressed by SGNs comes from *in vitro* studies of AMPA-mediated excitotoxic damage in which AMPA exposure causes Ca^{2+} entry into afferent neurons (Eybalin et al., 2004).

In the present work, structural and functional studies of mature rat and frog auditory synapses were conducted to demonstrate that CP-AMPARs are present and mediate glutamatergic transmission in the auditory organ. Calcium-imaging studies in the larval zebrafish provided mechanistic information linking CP-AMPARs with excitotoxic damage and suggest a strategy for protecting against hearing loss by limiting Ca^{2+} accumulation in the afferent terminal.

Materials and Methods

Zebrafish. All zebrafish experiments were approved by the University of Washington Institutional Animal Care and Use Committee. Fish were reared in E3 embryo medium containing the following (in mM): 14.97 NaCl, 0.5 KCl, 0.042 Na_2HPO_4, 0.15 KH_2PO_4, 1 $CaCl_2$, 1 $MgSO_4$, and 0.714 $NaHCO_3$, pH 7.2, at ~28.5°C. Experiments were performed on zebrafish larvae 6–7 dpf, a stage before sex is determined in this species, in extracellular solution containing the following (in mM): 130 NaCl, 2 KCl, 1 $MgCl_2$, 10 HEPES, and 2 $CaCl_2$ (Trapani and Nicolson, 2011). Fish were paralyzed via cardiac injection of α-bungarotoxin (125 μM; Trapani and Nicolson, 2010), which blocks skeletal muscle contraction while allowing the heart to continue beating. Briefly, fish were anesthetized by hypothermia, immobilized with a harp conventionally used for brain slices, and injected with α-bungarotoxin containing phenol red into the heart chamber. In a subset of imaging studies, fish were instead immobilized with 0.2% tricaine in E3. Extensive control experiments were conducted to determine whether tricaine affected waterjet responses, terminal morphology, and Ca^{2+} accumulation in the terminal. There were no differences between immobilization methods. When tricaine was used, it is indicated in the text.

Transgenic zebrafish lines. To assess hair cell and afferent terminal calcium responses to waterjet stimulation, *Tg[myo6b:GCaMP3]*^{w78Tg} (Esterberg et al., 2013) and *Tg[elavl3:GCaMP5G]*^{a4598Tg} (Ahrens et al., 2013) transgenic lines were used, respectively. To assess Ca^{2+} accumulation in afferent terminals, we used the *Tg[elavl3:GCaMP5G]* line. Given that *elavl3* is a pan-neuronal promoter, we also generated zebrafish that transiently expressed GCaMP3 only in posterior lateral line ganglion (pLLG) afferent neurons driven by the SILL1 enhancer *[hsp70l:GCaMP3-2.0cntnap2a]* (Pujol-Marti et al., 2012; see Fig. 9). To assess afferent and efferent terminal morphology, *Tg[neuroD:eGFP]*^{nl1Tg} (Obholzer et al., 2008) and *Tg[islet1:GFP]*^{rw0Tg} (Higashijima et al., 2000) transgenic lines were used, respectively.

Zebrafish electrophysiology. Paralyzed *Tg[neuroD:eGFP]* larvae were secured onto a Sylgard-coated coverslip with minimal application of WormGlu (GluStitch), and the fish and coverslip were transferred to a glass-bottom recording chamber coated with paraffin. Electrodes were filled with filtered extracellular solution. Loose-patch voltage-clamp recordings (series resistances, 20–80 MΩ) were obtained from individual neurons of the posterior lateral line ganglion visually identified using infrared differential interference contrast optics (Trapani and Nicolson, 2010). Data were acquired using pClamp10 software (Molecular Devices) at a gain of 10 and filtered at 5 kHz. After neuronal firing was recorded for at least 2 min, the chamber was bath perfused with different concentrations of AMPA. Series resistance was measured before and after each recording, and data were discarded if the resistance changed by >25%. Recordings were converted to text format then imported to MATLAB. Spike detection software in the Signal Processing Toolbox was used to quantify both spike frequency and interspike intervals.

Waterjet stimulation. Stereocilia of lateral line hair cells were displaced via application of a sinusoidal pressure wave (Trapani and Nicolson, 2011). A glass pipette (tip outer diameter, ~30 μm) was filled with an extracellular solution placed ~100 μm from the hair cell cluster termed a "neuromast," and deflection of the kinocilia was used to verify pressure wave administration. Pressure output was driven by a pressure clamp (HSPC-1, ALA Scientific) that was commanded by pClamp10 software. To assess hair cell or afferent terminal responses to hair cell activation, a 20 or 10 s, respectively, rectified 1 Hz pressure wave was applied. GCaMP fluorescence values was captured every 1–2 s for 1 min using Slidebook with the onset of waterjet stimulation 20 s into capture.

Pharmacology. AMPA, cyclothiazide (CTZ), and α-bungarotoxin (Tocris Bioscience) were used at the indicated concentrations. To examine the receptors and pathways that mediate calcium accumulation in the terminals, we used antagonists for AMPARs (DNQX, Sigma Aldrich), Ca^{2+}-permeable AMPARs [IEM1460 (hereon referred to as IEM); Tocris Bioscience], and NMDARs (APV, Sigma Aldrich).

Zebrafish time-lapse imaging and analysis. Images were acquired using an inverted Marianas spinning disk system (Intelligent Imaging Innovations) equipped with an Evolve 10 MHz EMCCD camera (Photometrics) and a Zeiss C-Apochromat 63×/1.2 numerical aperture (NA) water-objective. Camera intensification was set to keep exposure times to <100 ms for GFP and ~100 ms for GCaMP, while keeping pixel intensity at <25% of saturation. Camera gain was set at 3 to minimize photobleaching. GFP and GCaMP fluorescence were acquired with a 488 nm laser and a 535/30 emission filter.

Given that all *in vivo* imaging studies were conducted on an inverted microscope, fish were oriented in two different ways for experiments in which we assayed terminal structure and Ca^{2+} accumulation versus waterjet responses. Fish were oriented with the dorsal side toward the microscope for all waterjet experiments. This enabled stimulation of the hair cell with the waterjet pipette and simultaneous imaging of the terminals. Terminals of P1–3 neuromast terminals were imaged from the side, and the D1 neuromast terminal was captured from the top down due to its more dorsal location. To assay terminal structure and quantify Ca^{2+} accumulation, fish were placed with their sides flush against the objective to optimize visualization of the terminal structure.

To examine morphological changes or Ca^{2+} levels in afferent terminals in response to AMPA application, *Tg[neuroD:eGFP]* or *Tg[elavl3:GCaMP5G]* fish were immobilized with a harp. z-Sections were taken at intervals of 0.5–1 μm through the depth of the neuromast, including the afferent terminal, typically 20 μm. The *z*-sections were acquired before treatment, AMPA or DMSO was added directly to the imaging chamber, and images were acquired after 15 min of treatment. AMPA or DMSO was washed out of the chamber via a gravity perfusion system, and *z*-sections were again acquired 90 min postwash. Maximum projections in the untreated, AMPA, or DMSO condition, and if relevant, the wash condition were aligned using the Fiji StackReg plugin.

To monitor morphological changes in efferent terminals, the process was repeated with 6–7dpf *Tg[Islet1:GFP]* fish without a wash and recovery period. For analyses of morphological change, *z*-sections of *Tg[neuroD:eGFP]*- or *Tg[Islet1:GFP]*-labeled processes were opened in the Fiji Simple Neurite Tracer (SNT). Neuritic processes of afferent and efferent terminals were traced for each of the treatment conditions (afferent: control, AMPA, and wash; efferent: control and wash). Using the maximum projection image for each condition, processes were traced starting from the first branch point along the axon to the most distal point that likely represented a postsynaptic terminal. Each neurite was traced from a branch point to the distal most pixel identified by SNT. SNT only traced neurites represented by a continuous segment of bright pixels. Terminal swelling often caused breaks in this continuous segment or shortening of the neuritic branch. All values were converted to microns using the appropriate calibration for the microscope settings. Mean branch length and number of branches were computed for each terminal in the treatment conditions.

To assess hair cell and afferent terminal calcium responses to waterjet stimulation, hair cells or terminals were identified that consistently responded to at least two stimulation trials, AMPA was applied to the imaging chamber for at least 15 min, and two stimulation trials were repeated. For all hair cell-imaging experiments, a single hair cell was analyzed for each *Tg[myo6b:GCaMP3]* fish ($n = 7$ fish). The region of interest was drawn around the entire hair cell that showed a response. For all terminal imaging, a single terminal was imaged in each *Tg[elavl3:GCaMP5G]* fish, and the entire region of the terminal shown in the focal plane was designated as the region of interest. To assay the recovery of afferent terminal responses, AMPA was washed out of the imaging chamber for at least 60 min, and the stimulation trials were repeated.

For analyses of waterjet hair cell and terminal responses, fluorescence intensity was quantified using SlideBook software (Intelligent Imaging Innovations) and GCaMP fluorescence measurements were exported to MATLAB. As described previously (Esterberg et al., 2013), fluorescence data are normalized by dividing the fluorescence intensity values for the entire acquisition period by the baseline value before waterjet stimulation. Using baseline-adjusted traces, the peak of each calcium response was computed. To compute the half-width of each trace as a measure of response duration, traces were first normalized to peak. Each data point in the control, AMPA-treated, and recovery conditions represents the mean of two GCaMP responses to a pressure wave.

Zebrafish whole-mount immunohistochemistry and fluorescence imaging. All zebrafish immunohistochemistry experiments were approved by the Massachusetts Eye and Ear Institutional Animal Care and Use Committee (IACUC). The 5-d-old larvae were exposed to 100 μM (S)-AMPA (Abcam) diluted in E3 embryo media with 0.1% DMSO for 15 min at room temperature (20–22°C). E3 with 0.1% DMSO were used as controls. Following drug exposure, larvae either were immediately fixed for immunohistochemistry or were allowed to recover for 1 h. Larvae were quickly sedated on ice then transferred to fixative (4% paraformaldehyde/4% sucrose/0.15 mM CaCl2 in phosphate buffer) for 1 h. Following fixation, larvae were permeabilized in 1% Tween in PBS for 5 h at 4°C then blocked in PBS buffer containing 1% bovine serum albumin, 0.5% Fish Skin Gelatin, 2% goat serum, and 0.1% DMSO for >3 h. The following antibodies were used: MAGUK (K28/86; 1:500); GluA4 (1:400; Millipore Bioscience Research Reagents); and an affinity-purified antibody generated against zebrafish Ribeye b (mouse IgG2a; 1:2000; Sheets et al., 2011). Primary antibodies were diluted in blocking buffer and applied overnight at 4°C followed by diluted secondary antibodies coupled to Alexa Fluor 488 and Alexa Fluor 647 (Invitrogen), or DyLight 549 (Jackson ImmunoResearch), and labeled with DAPI (Invitrogen). *z*-Stack images of neuromasts (spaced by 0.3 μm over 10–12 μm) were acquired with a Leica SP8 confocal microscope using a 63×/1.3 NA glycerol immersion objective lens. For each experiment, the microscope parameters were adjusted using the brightest control specimen. Digital images were processed using ImageJ software and Amira 3D software (FEI).

Quantitative image analysis was performed on raw images using Amira 3D Analysis software as previously described (Lv et al., 2016). To quantitatively measure immunolabel intensity, a user-defined inclusive threshold was applied to isolate pixels occupied by GluA4 or postsynaptic density (PSD)-immunolabeled patches. The inclusive threshold values for each label were determined using 3D isosurface renderings, with the minimum threshold value defined as the value above which the user could resolve two closely adjacent patches. The material statistics function was then used to measure the cumulative intensity of fluorescent pixels (sum of the grayscale values) within each individual sphere or patch as well as to define the *x*-, *y*-, and *z*-coordinates of the center of each puncta within the stack. Postsynaptic Gria4-immunolabeled clusters were identified as Gria4 labeling that generally overlapped with the MAGUK immunolabel.

Rat iGluR staining. All rat experiments were approved by the IACUC at Washington University in St. Louis. Immunohistochemistry on mature Wistar rats of either sex was performed as previously described (Jing et al., 2013; Kim and Rutherford, 2016). Cochlear whole-mount samples were used to image the PSDs of type I auditory nerve fibers in the organ of Corti on a Zeiss LSM 700 microscope with a 63× 1.4 NA oil-immersion objective. Pixels were 50 × 50 nm, and the *z*-step was 333 nm.

Three AMPA receptor subunits were labeled simultaneously with primary antibodies against GluA2 (mouse IgG2a, catalog #MAB397, Millipore; Vissavajjhala et al., 1996), GluA3 (goat, sc-7612, Santa Cruz Biotechnology), or GluA4 (rabbit, catalog #AB1508, Millipore; Wenthold et al., 1992). Specificity of the GluA2 and GluA4 antibodies (Medvedev et al., 2008; Sagata et al., 2010) were verified in GluA2 and GluA4 knock-out mice (Jia et al., 1996; Sagata et al., 2010), respectively. We find no reference for use of the GluA3 antibody on the GluA3 knock-out mouse; however, sc-7612 has been used previously with the GluA4 antibody AB1508 for immunohistochemistry on retinal ribbon synapses with similar results (Puller and Haverkamp, 2011; Puthussery et al., 2014). Secondary antibodies were Alexa Fluor 488 anti-goat, Alexa Fluor 555 anti-rabbit, and Alexa Fluor 647 anti-mouse. Imaris software (Bitplane) was used for 3D analysis of synaptic punctum intensity and volume. We note that differences in the levels of subunit immunofluorescence potentially result from differences in the binding efficiency of the antibodies, and thus acquiring three channels with the same microscope settings would not be expected to produce fluorescence ratios that indicate absolute measurements of subunit relative abundance at a given synapse. Therefore, to maximize the dynamic range of level detection during acquisition, the microscope settings on each of the three channels in an image

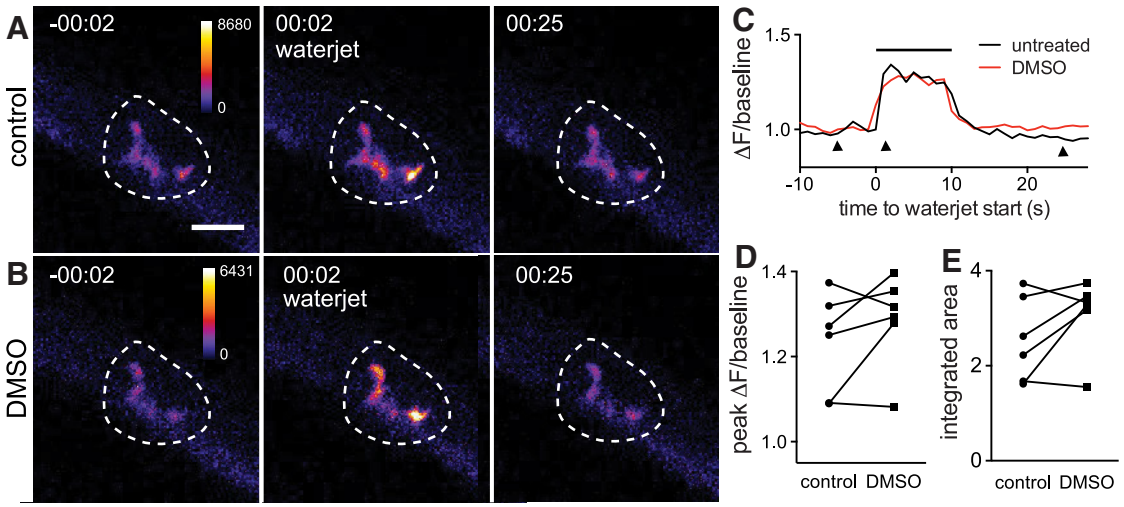

Figure 1. Waterjet-mediated hair cell stimulation causes afferent terminal Ca^{2+} entry. *Tg[elavl3:GCaMP5G]* transgenic line was used to measure responsiveness of afferent terminal to waterjet-mediated displacement of hair cell stereocilia. ***A***, ***B***, Frames from a time-lapse video (1 s capture interval) before, during, and after waterjet stimulation are shown in the control condition (***A***) and following DMSO application (***B***). Dashed line marks the location of the terminal and thereby the region of interest used for analysis. Scale bar, 10 μm. ***C***, Representative traces showing changes in the fluorescence intensity normalized to baseline. Horizontal line starting at time = 0 marks the duration of the waterjet stimulus. ***D***, ***E***, Summary data of mean peak and integrated area of the response in the control and DMSO condition (n = 6 fish, 1 terminal/fish). Paired t test.

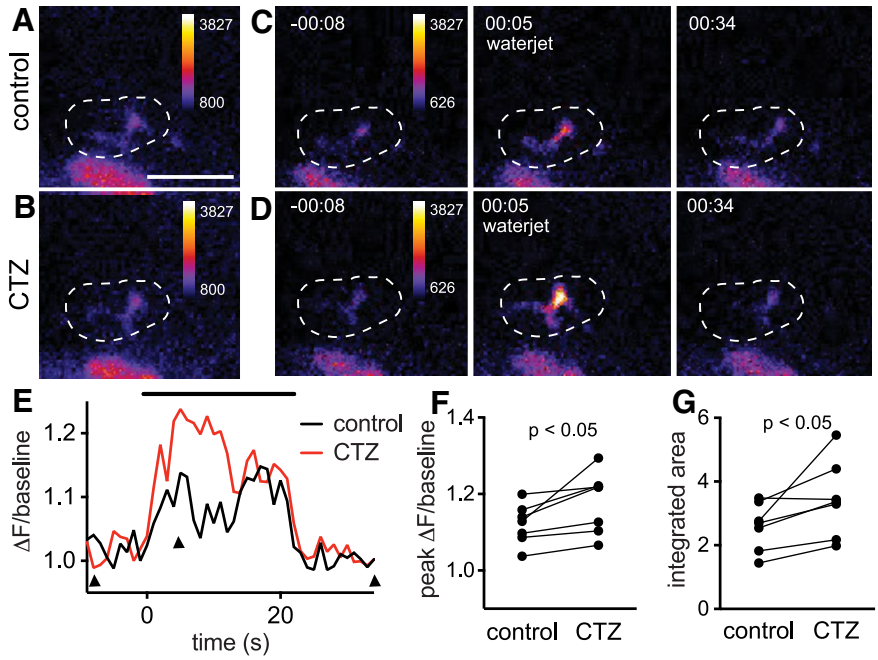

Figure 2. Perfusion of CTZ enhances terminal responsiveness to hair cell activation. *Tg[elavl3:GCaMP5G]* transgenic line was used to measure the responsiveness of the afferent terminal to waterjet-mediated displacement of hair cell stereocilia. ***A***, ***B***, Maximum projections of an afferent terminal in the control condition (***A***) and with CTZ (***B***). ***C***, ***D***, Frames from a time-lapse video (1 s capture interval) before, during, and after waterjet stimulation are shown in the untreated condition (***C***) and following CTZ application (***D***). The dashed line marks the location of the terminal and thereby the region of interest used for analysis. Scale bar, 10 μm. ***E***, Representative traces showing changes in the fluorescence intensity normalized to baseline. ***F***, ***G***, CTZ increases the peak and integrated area of the waterjet response. Paired t test.

volume were adjusted to have level saturation at the brightest pixel of the brightest synapse. This normalization resulted in synapses with similar overall intensities on each channel. IGOR software (WaveMetrics) was used for line plots on the 2D maximum-intensity projections of postsynaptic densities oriented en face. Images in Figure 1I were deconvolved, to reduce blur, with an optical model of the point spread function in ImageJ software as previously described (Jing et al., 2013; Ohn et al., 2016).

To control for artifacts due to bleaching and attenuation in our experimental system, we coated coverslips with fluorescent beads and mounted the tissue between two coverslips so that the sample and the beads on both sides can be imaged and measured from either side. Attenuation makes synapses closer to the coverslip appear brighter. Assuming a linear trend, we estimate the effects of attenuation in the whole mount to be <5% for synapses separated by <20 μm along the z-axis. Local deviations in volume and intensity between synapses (i.e., between synapses centered within 333 nm from each other) far exceed the size of the linear trend across the ~20 μm range of the synaptic layer, suggesting that true morphological heterogeneity dominates these differences in luminance values. Fluorophores outside the focal plane can be bleached, leading to artifacts that depend upon the order of acquisition when scanning through Z. To control for bleaching, we scanned the volume twice and calculated the rate of bleaching for each channel by comparing the synaptic intensities from scan 1 with the synaptic intensities from scan 2. For GluA3 and GluA4, the fraction of retained fluorescence (the mean synaptic intensity on scan 2 divided by the mean synaptic intensity on scan 1) was >0.95. For the GluA2 signal in the volume in Figure 1*B*, after 40 sections the retained fluorescence fraction was 0.70, which was used to calculate the mean retained fraction per scan as the 40th root of 0.7 = 0.991. The bleaching trend was then subtracted from the data for each subunit for each synapse before plotting data in Figures 1 and 2. For GluA2 per synapse, the Corrected Intensity = Measured Intensity/(0.991^section#), where section# was calculated as the center of the synapse in Z.

Electrophysiology from adult bullfrog auditory hair cells. All frog experiments were approved by the IACUC at Oregon Health & Science University. Amphibian papillae of adult female or male bullfrogs (*Rana catesbeiana*) were carefully dissected and, as previously described (Keen and Hudspeth, 2006; Li et al., 2009), semi-intact preparations of hair cells and their corresponding afferent fibers were obtained. During the re-

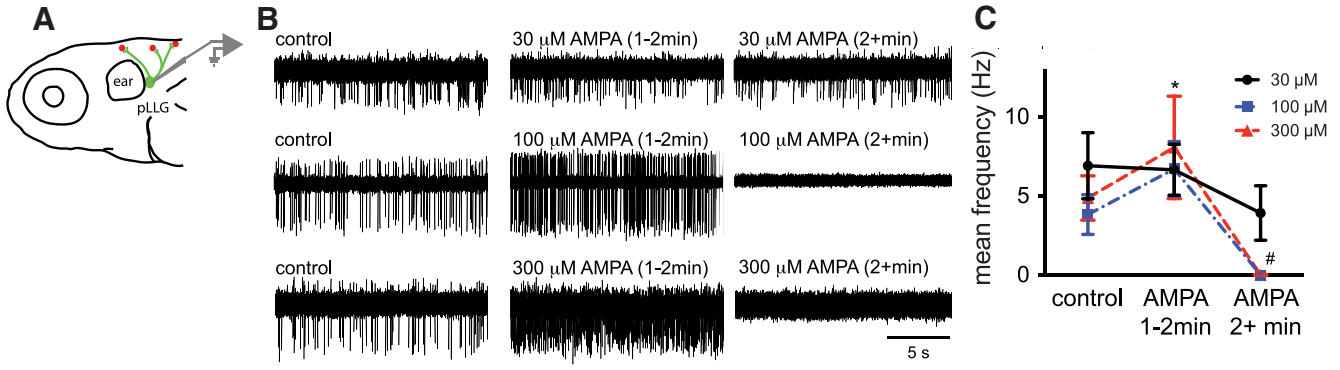

Figure 3. AMPA perfusion diminishes afferent neuron firing in a dose-dependent manner. ***A***, Schematic showing zebrafish head and the location of the pLLG just caudal to the ear. Loose-patch voltage-clamp recordings were obtained from cell bodies in the pLLG (green), which receive glutamatergic inputs from clusters of hair cells (red). ***B***, Representative traces of pLLG neuron firing in ambient conditions (control) and following bath application of varying doses of AMPA. AMPA (100 and 300 μM) caused a statistically significant transient increase in firing frequency in many cells during the first 1–2 min of application (*$p < 0.05$) followed by a dramatic reduction in firing (#$p < 0.001$). ***C***, Summary data show that the mean firing frequency decreases dramatically following 100 μM ($n = 9$ cells) and 300 μM ($n = 6$ cells) AMPA application but not 30 μM AMPA ($n = 8$ cells). Two-way ANOVA.

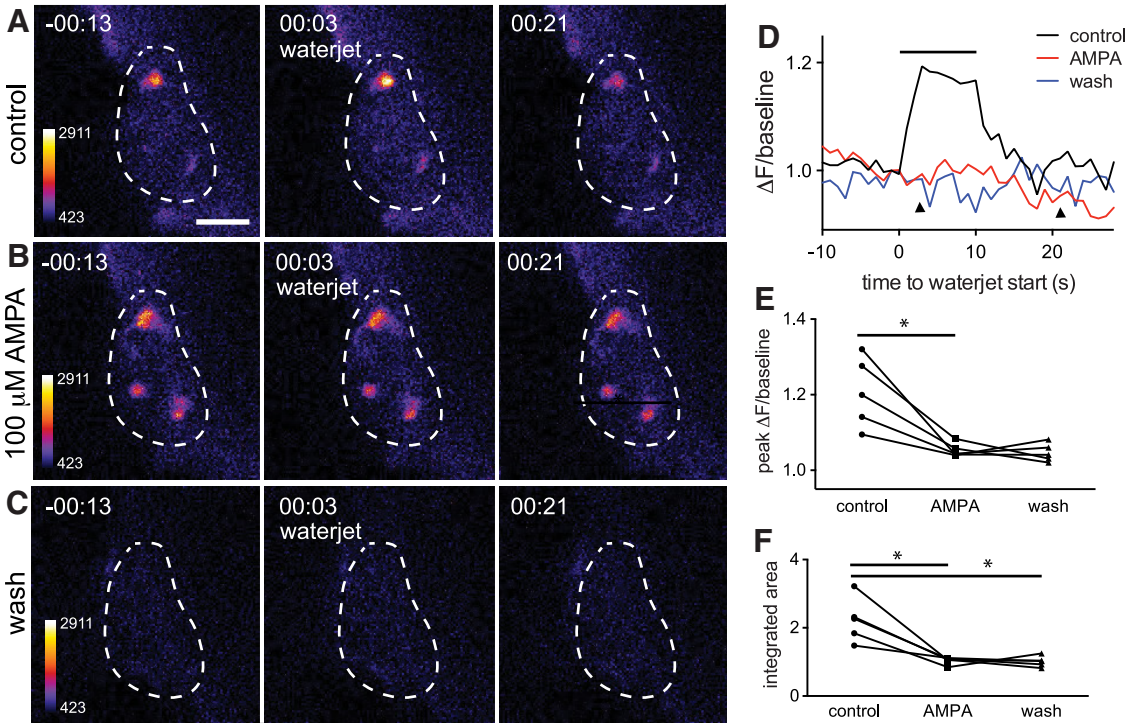

Figure 4. Perfusion of 100 μM AMPA diminishes terminal responsiveness to hair cell activation. The *Tg[elavl3:GCaMP5G]* transgenic line was used to measure the responsiveness of afferent terminal to waterjet-mediated displacement of hair cell stereocilia. ***A–C***, Frames from a time-lapse video before, during, and after waterjet stimulation are shown in the control condition (***A***), following 100 μM AMPA application (***B***), and 2 h after wash (***C***). The dashed line marks the location of the terminal and thereby the region of interest used for analysis. Scale bar, 10 μm. ***D***, Response to waterjet is diminished following AMPA application and wash. ***E***, ***F***, Summary data of the mean peak and integrated area of the response in the control, AMPA, and wash conditions. One-way ANOVA, *$p < 0.05$.

cordings, the preparation was perfused (2–3 ml/min) with oxygenated artificial perilymph containing the following (in mM): 95 NaCl, 2 KCl, 2 $CaCl_2$, 1 $MgCl_2$, 25 $NaHCO_3$, 3 glucose, 1 creatine, and 1 Na-pyruvate, pH 7.30, 230 mOsm. For paired recordings, patch pipettes of borosilicate glass were pulled to resistances of 5–6 MΩ for hair cells and 7–10 MΩ for afferent fibers. Pipettes were filled with the internal solution containing the following (in mM): 77 Cs-gluconate, 20 CsCl, 1 $MgCl_2$, 10 TEA-Cl, 10 HEPES, 2 EGTA, 3 Mg-ATP, 1 Na-GTP, and 5 Na_2-phosphocreatine, pH 7.30, 230 mOsm. Whole-cell recordings were performed at room temperature using an EPC-10/2 amplifier (HEKA) and Patchmaster software (HEKA). Both hair cells and afferent fibers were voltage clamped with a resting membrane potential of −90 mV after liquid junction potential correction. The current signal was low-pass filtered at 5 kHz and sampled at 10 μs intervals. The averaged uncompensated series resistances in whole-cell recordings were 12.6 ± 1.0 MΩ for hair cells ($n = 16$) and 23.8 ± 2.8 MΩ for afferent fibers ($n = 16$). The measurements of the whole-cell membrane capacitance (C_m) from hair cells were performed under voltage clamp with the "Sine + DC" method (Lindau and Neher, 1988; Gillis, 2000) using an EPC-10/2 patch-clamp amplifier (HEKA) and Pulse software (HEKA). Sine waves (50 mV peak-to-peak, 1 or 2 kHz) were superposed on the holding potential, and the resulting current response was used to calculate C_m via a Pulse software emulator of a lock-in amplifier (Gillis, 2000). Data analysis was performed with Igor Pro software (WaveMetrics). Data are expressed as the mean ± SEM.

Statistics. GraphPad Prism 5.0 Software was used for all statistical analyses. ANOVAs used the Tukey *post hoc* test.

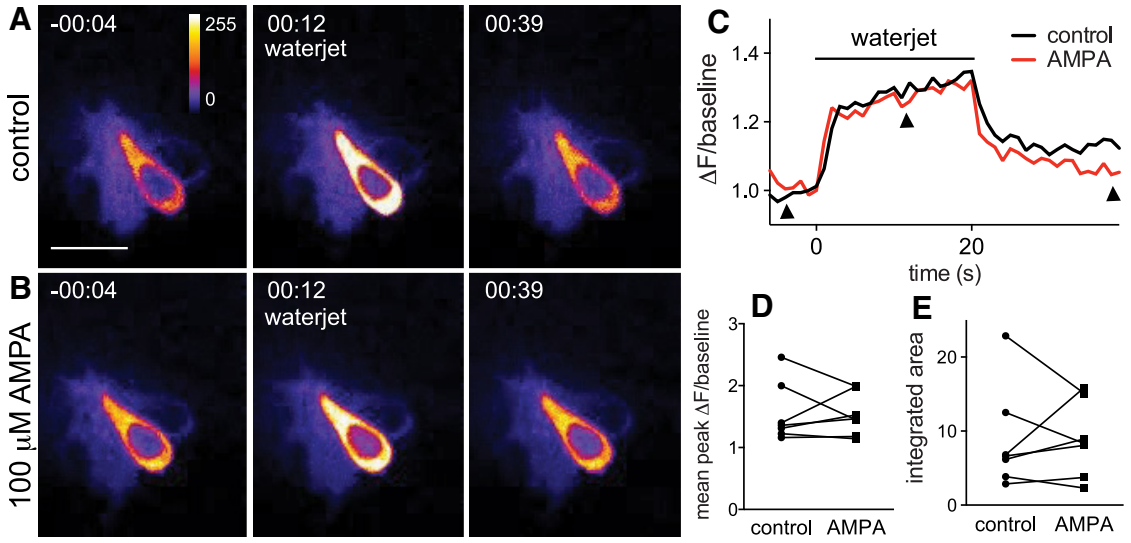

Figure 5. AMPA does not affect hair cell mechanotransduction. ***A***, Frames from a time-lapse calcium-imaging video acquired from *Tg[myo6b:GCaMP3]* fish. GCaMP3 fluorescence is shown in the control condition (top) before, during, and after waterjet stimulation (left, middle, and right, respectively). ***B***, Images represent the same sequences during AMPA exposure. ***C***, GCaMP3 responses to waterjet in the control and AMPA condition. Arrowheads mark the time points shown in ***A*** and ***B***. ***D***, ***E***, Summary data of the mean peak and integrated area of the waterjet responses. Each point is an average of two to three trials. Control and AMPA data are paired. AMPA does not significantly affect the waterjet response. Scale bar, 10 μm.

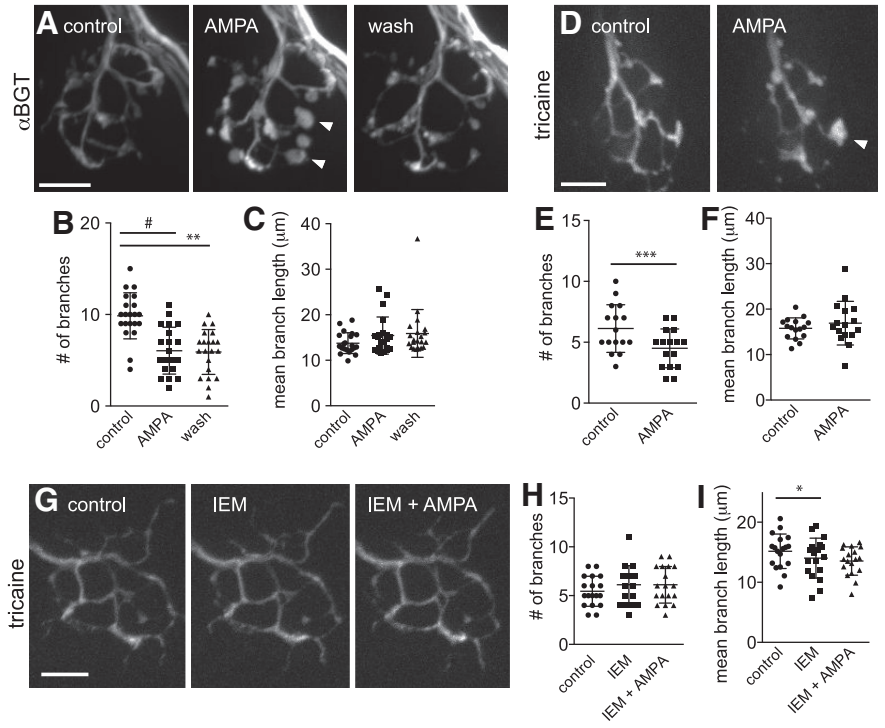

Figure 6. AMPA causes morphological changes to afferent terminals that is prevented by blocking CP-AMPARs. ***A***, Maximum projections of a *Tg[neuroD:GFP]* afferent terminal in the control condition following bath perfusion of 100 μM AMPA and 90 min of wash. Fish were immobilized with alpha-bungarotoxin (a-BGT). ***D***, Maximum projections in control and following AMPA treatment. ***A***, ***D***, Fish were immobilized with tricaine. In the AMPA images (***A***, middle; ***D***, right), arrowheads indicate some of the terminal swellings. ***B***, ***C***, ***E***, ***F***, Regardless of the immobilization method, AMPA caused a decrease in the number of branches (***B***, ***E***), while the mean branch length (***C***, ***F***) is unchanged. Scale bars, 10 μm. ***G***, Maximum projections of a terminal in the control condition, following IEM application and IEM + AMPA (100 μM). IEM prevented AMPA-mediated changes to terminal morphology. ***I***, However, IEM alone reduced the mean branch length. *$p < 0.05$, **$p < 0.001$, ***$p < 0.01$, #$p < 0.0001$.

Results

In vivo hair cell stimulation causes Ca^{2+} influx into afferent terminals

To examine the contribution of AMPARs to glutamatergic transmission at the hair cell synapse, we used *in vivo* time-lapse Ca^{2+} imaging in the larval zebrafish lateral line. We visualized afferent terminal responses to hair cell stereocilia deflection using the *Tg[elavl3:GCaMP5G]* line in which the Ca^{2+} indicator GCaMP5 is expressed pan-neuronally, including in afferent neurons. Stereocilia were displaced for 20 s using a 1 Hz rectified pressure wave administered via a waterjet pipette placed ~100 μm away from the neuromast. Figure 1 shows frames from time-lapse videos with single planes of afferent terminals before, during, and after waterjet stimulation. Under control conditions, GCaMP5 fluorescence intensity increases, indicating that hair cell activation causes an influx of Ca^{2+} into the terminal (Fig. 1*A*,*F*). The response to waterjet stimulation was quantified by measuring the mean peak fluorescence and duration of the response across two waterjet stimulation trials.

AMPARs desensitize at a faster time course relative to NMDA and kainate receptors (Geiger et al., 1995), a process that can be studied using the drug CTZ, which blocks AMPAR desensitization (Trussell et al., 1993). Bath application of 200 μM CTZ had no detectable effect on GCaMP fluorescence under resting conditions, as shown in maximum projections of a *z*-stack of a terminal before and after CTZ application (Fig. 2*A*,*B*). In contrast, CTZ (200 μm) enhanced the terminal waterjet responses as shown in the time-lapse video frames (Fig. 2*C*,*D*) and the plot of fluorescence intensity over time (Fig. 2*E*). CTZ increases the mean peak (control, 1.12 ± 0.02; CTZ, 1.18 ± 0.02; $n = 7$, $p < 0.05$, mean ± SEM, paired *t* test; Fig. 2*F*) and integrated area (con-

trol, 2.6 ± 0.3; CTZ, 3.4 ± 0.5; $n = 7$, $p < 0.05$, mean ± SEM; Fig. 2*G*) of the waterjet responses.

We attempted to determine whether the terminal Ca^{2+} responses are mediated by CP-AMPARs using an antagonist that specifically blocks these receptors, IEM (Kim and von Gersdorff, 2016). We imaged waterjet responses before and after bath application of 100 μM IEM or DMSO carrier. DMSO does not substantially change the mean integrated area (control, 2.6 ± 1.0; DMSO, 3.1 ± 1.3; $n = 6$, $p = 0.15$, mean ± SEM) of the terminal response. In contrast, IEM significantly diminished terminal waterjet responses as shown in the time-lapse video frames and the plot of fluorescence intensity over time. IEM decreased the mean integrated area (control, 3.5 ± 0.6; IEM, 1.1 ± 0.09; $n = 5$, $p < 0.05$, mean ± SEM) of the waterjet responses. However, imaging of hair cell waterjet responses using *Tg[myo6b:GCaMP3]*^{w78} revealed that IEM (50 and 100 μM) also blocks hair cell responses (control, 4.5 ± 0.8; IEM, 1.3 ± 0.1; $n = 6$, $p < 0.05$, mean ± SEM). Fortunately, the bullfrog model system was better suited to examine the contribution of CP-AMPARs to glutamatergic transmission at the hair cell synapse (see Fig. 12). However, we continued using the zebrafish model system to examine the contribution of CP-AMPARs to excitotoxic damage.

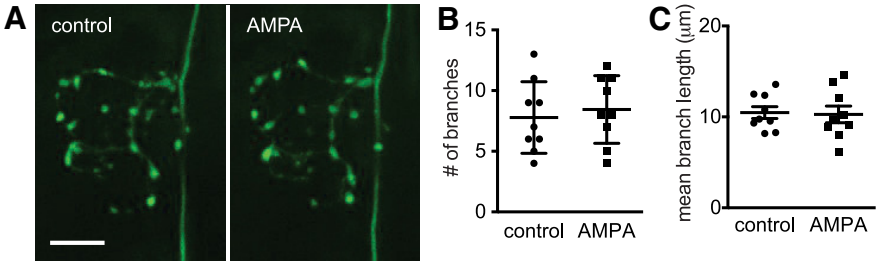

Figure 7. AMPA does not affect efferent terminal morphology. ***A***, Maximum projection images of efferent terminals from *Tg[Islet1:GFP]* fish (6 dpf) before and during 100 μM AMPA exposure. Scale bar, 10 μm. ***B***, ***C***, AMPA exposure did not change the number of branches (***B***) or the mean branch length (***C***). Each data point represents a measurement taken from a single terminal. Error bars indicate the SD in ***B*** and SEM in ***C***.

Afferent neurons lose responsiveness after exposure to exogenous AMPA

We conducted a series of electrophysiological and Ca^{2+} imaging experiments to determine whether CP-AMPARs mediate excitotoxic damage. First, we examined the effect of AMPA application on the overall activity of posterior lateral line ganglion neurons by recording presynaptically driven spontaneous spike firing. The range of concentrations was chosen based on dose-response studies in mammalian cochlea (Puel et al., 1991, 1994). In Figure 3*A* is a schematic of a larval zebrafish head showing the location of the recording electrode used to obtain loose-patch voltage-clamp recordings from individual pLLG neurons. Figure 3*B* shows representative action current recordings before and after the perfusion of varying concentrations of AMPA. Application of 100 or 300 μM AMPA caused a brief bout of high-frequency spiking before firing diminished (Fig. 3*B*, middle panels). We observed the initial increase in spiking in six of nine neurons and the decrease in all neurons analyzed. The AMPA concentration of 100 μM was the lowest dose tested that reduced mean firing frequency (Fig. 3*C*).

We next examined how the response of afferent terminals to waterjet stimulus is altered by AMPA treatment. We imaged waterjet responses in a terminal in the untreated condition, following bath application of 100 μM AMPA and 2 h after wash (Fig. 4*A–C*). We noted that AMPA exposure increased the baseline fluorescence in terminals, examined further below. However, after AMPA exposure there was little or no increase in terminal fluorescence in response to waterjet. AMPA decreased the mean peak (Fig. 4*E*; control, 1.2 ± 0.5; AMPA, 1.1 ± 0.5; wash, 1.0 ± 0.5; $n = 6$, mean ± SEM, one-way ANOVA; control vs AMPA, $p < 0.05$) and integrated area (Fig. 4*F*; control, 2.2 ± 1.0; AMPA, 1.0 ± 0.5; wash, 1.0 ± 0.5; $n = 6$, mean ± SEM, one-way ANOVA; control vs AMPA, $p < 0.05$; control vs wash, $p < 0.05$) of the terminal response, and these values did not recover after wash.

While these results are consistent with AMPA overexposure resulting in postsynaptic dysfunction, it is possible that AMPA disrupted neuronal firing indirectly by acting on the presynaptic hair cell. To address whether AMPA exposure altered the hair cell response to mechanical stimuli, we conducted *in vivo* Ca^{2+}-imaging studies using the *Tg[myo6b:GCaMP3]*^{w78} fish, which express GCaMP3 in the hair cell cytoplasm during and after waterjet exposure (Fig. 5). Under control conditions, increases in fluorescence intensity temporally correlate with the duration of waterjet stimulation. AMPA did not substantially change either the mean peak (control, 1.6 ± 0.2; AMPA, 1.5 ± 0.1; $n = 7$, $p = 0.9$, mean ± SEM) or integrated area (control, 8.8 ± 2.6; AMPA, 8.9 ± 2.0; $n = 7$, $p = 0.97$, mean ± SEM) of the hair cell Ca^{2+} response to mechanical displacement, suggesting that presynaptic Ca^{2+} signals were maintained during AMPA exposure and that loss of responsiveness was mediated postsynaptically.

Exogenous AMPA exposure results in excitotoxic damage that involves CP-AMPARs

Our observation that AMPA exposure caused a loss of terminal responsiveness suggested that the terminal sustained excitotoxic damage. One characteristic of such damage in the mammalian cochlea is a swelling of afferent SGN terminals (Puel et al., 1991, 1994, 1998). We conducted *in vivo* time-lapse imaging of the *Tg[neuroD:eGFP]* transgenic line, which labels afferent terminals before, during application of 100 μM AMPA, and 90 min after washout (Fig. 6). During AMPA application, terminals exhibited swelling consistent with mammalian observations. In the panel of images shown in Figure 6*A*, these swellings are marked by the arrowheads in the AMPA treatment condition (Fig. 6*A*, middle). The number of neuritic branches in each terminal decreased during AMPA treatment (control, 9.9 ± 0.6; AMPA, 6.1 ± 0.6; wash, 6.0 ± 0.5; $n = 21$, mean ± SD; ANOVA, $p < 0.0001$) while the mean neuritic branch length remained the same (control, 13.8 ± 0.5 μm; AMPA, 15.5 ± 0.9 μm; wash, 15.9 ± 1.1 μm; $n = 21$, mean ± SEM). Following 90 min of washing, neither measure of terminal morphology recovered. Figure 6*A--F* represent data acquired in larvae immobilized with α-bungarotoxin versus tricaine. In the presence of tricaine (Fig. 6*D--F*), the number of branches decreased during AMPA (control, 6.1 ± 0.5; AMPA, 4.5 ± 0.4; $n = 16$, mean ± SD; paired *t* test, $p < 0.001$) while the mean branch length remained the same (control, 15.7 ± 0.6 μm; AMPA, 17 ± 1.2 μm; $n = 16$, mean ± SEM). The immobilization method did not affect AMPA-mediated changes in terminal morphology. Blocking CP-AMPARs via bath application of IEM before 100 μM AMPA treatment prevented changes to the number

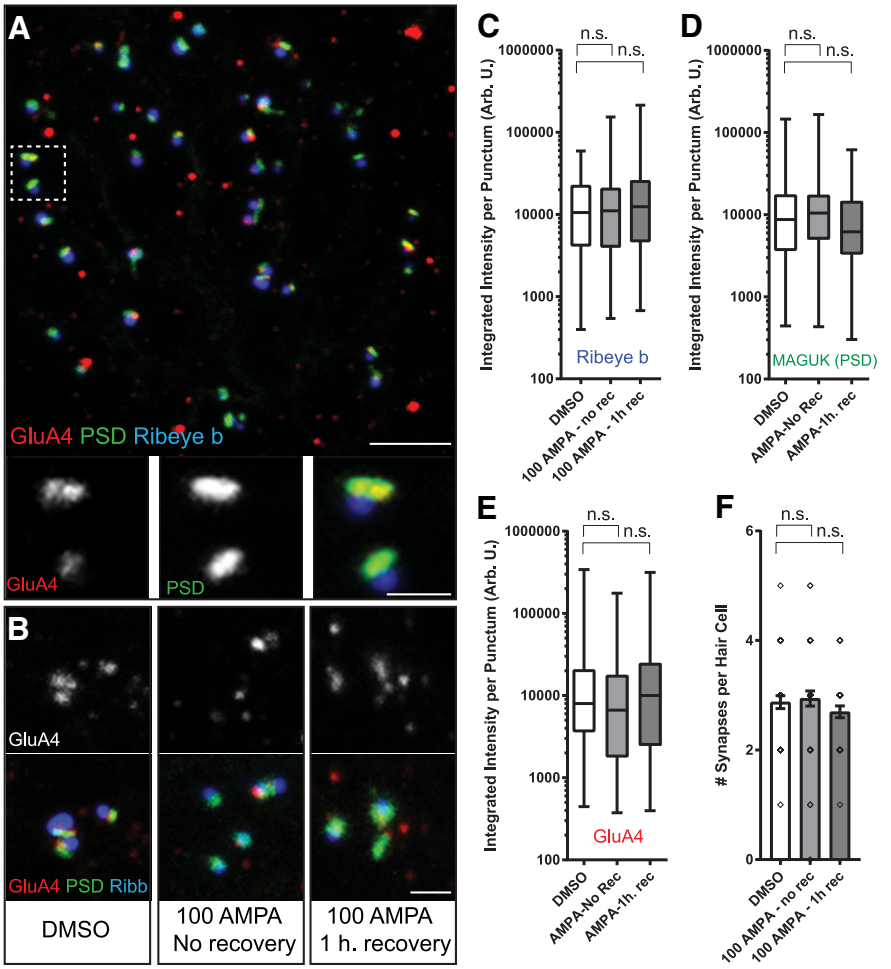

Figure 8. Postsynaptic markers following AMPA exposure. ***A***, Representative maximum intensity top-down (*x–y*) projection of GluA4 (red), afferent PSD (green) and synaptic ribbon (Ribeye b, blue) immunolabeled in a zebrafish neuromast at 5 dpf. Insets correspond to the boxed region of interest in ***A*** and highlight overlapping GluA4 and PSD immunolabels. Scale bars: ***A***, 3 μm; insets, 1 μm. ***B***, Representative thumbnail images of ribbon synapses in hair cells exposed to DMSO alone or 100 μM AMPA for 15 min then fixed immediately or allowed to recover for 1 h. Scale bar, 1 μm. ***C–E***, Box plots of integrated presynaptic Ribeye b (***C***), MAGUK PSD (***D***), and GluA4 subunit (***E***) immunolabel intensities. Each plot represents a population of intensity measurements of an individual labeled punctum collected from six to eight individual neuromasts (four to five individual larvae) per condition. Whiskers indicate the minimum and maximum values. Intensities of Ribeye b, GluA4, and PSD immunolabels are not significantly different between conditions (defined by the Dunn's multiple comparison test). ***F***, An aligned dot plot showing the number of intact synapses per individual neuromast hair cell. Bars represent the means; error bars indicate the SEM. An intact synapse was defined as Ribeye-immunolabeled puncta partially overlapping PSD puncta. Number of intact synapses per hair cell are not significantly different between conditions (defined by Dunnett's multiple-comparison test). Hair cell $n = 50$ (DMSO), $n = 61$ (AMPA, no recovery), and $n = 43$ (AMPA, 1 h recovery).

of branches (control, 5.4 ± 0.4 μm; IEM, 6.1 ± 0.5 μm; IEM plus AMPA, 6.1 ± 0.4 μm; $n = 18$, mean ± SEM). IEM treatment alone slightly reduced the mean branch length relative to control (control, 15 ± 1 μm; IEM, 14 ± 1 μm; IEM plus AMPA, 14 ± 1 μm; $n = 18$, mean ± SEM; ANOVA, $p < 0.05$). Representative images (Fig. 6*G*) and summary data (see Fig. 9*H*,*I*) for the control, IEM, and IEM plus AMPA conditions are shown.

We also examined whether AMPA causes any gross morphological changes to the presynaptic efferent terminals that are thought to play an inhibitory modulatory role at this synapse. We monitored the morphology of efferent terminals using time-lapse imaging experiments of *Tg[Islet1:GFP]*. Maximum projections of an efferent terminal are shown in Figure 7*A* before and during 100 μM AMPA exposure. There were no changes in the number of branches (control, 8 ± 3; AMPA, 8 ± 3; $n = 9$, mean ± SD) or mean branch length (control, 10 ± 0.6 μm; AMPA, 10 ± 1 μm; $n = 9$, mean ± SEM) in the presence of AMPA (Fig. 7*B*,*C*), demonstrating that efferent synapses were relatively insensitive to AMPA exposure.

To determine whether the distribution of synapses was altered after AMPA overexposure, we conducted triple immunolabeling of the presynaptic protein Ribeye, postsynaptic density MAGUK, and the GluA4 subunit (Fig. 8). Although *gria2a* and *gria2b*, encoding for GluA2 subunits, are expressed in the zebrafish lateral line ganglia (Hoppmann et al., 2008), commercial GluA2 antibodies do not cross-react with zebrafish. AMPA treatment had little effect on the expression of GluA4 nor did it change the distribution of Ribeye- and GluR-expressing puncta, suggesting that this AMPA exposure silenced synapses without their physical disassembly.

As noted earlier, we observed that terminals treated with AMPA exhibit an overall baseline increase in GCaMP fluorescence intensity while at the same time blocking response to waterjet stimuli. We quantified the percentage change in GCaMP fluorescence intensity following bath application of increasing concentrations of AMPA, compared with untreated terminals or those treated with DMSO carrier alone. While the application of DMSO alone or with 10 or 30 μM AMPA had no effect on GCaMP5 fluorescence of terminals (Fig. 9*A*,*B*,*I*), treatment with 100 and 300 μM AMPA (Fig. 9*C*,*D*,*I*) resulted in robust increases in fluorescence intensity relative to the untreated condition.

To determine which glutamatergic receptors mediate Ca^{2+} accumulation, we quantified the GCaMP fluorescence levels after a 15 min application of 100 μM AMPA in the presence of glutamate receptor blockers. Pretreatment with 40 μM DNQX, an antagonist for the AMPA and kainate receptors, blocked the increase in terminal GCaMP fluorescence levels that are observed following AMPA exposure (Fig. 9*E*,*I*). In contrast, NMDAR blockade using 50 μM APV was not able to block AMPA-mediated accumulation of terminal Ca^{2+}. We next examined whether blocking only CP-AMPARs can protect the terminal from Ca^{2+} accumulation and putative excitotoxic damage. At all doses tested, the CP-AMPAR blocker (IEM) was sufficient to either reduce or block AMPA-mediated increases in GCaMP fluorescence (Fig. 9*H*,*K*). To further demonstrate that AMPA causes Ca^{2+} accumulation in pLLG afferent neurons that is prevented by blocking CP-AMPARs, we generated transgenic zebrafish that transiently express GCaMP3 in pLLG neurons. AMPA (100 μM) caused a significant increase in fluorescence intensity that was prevented by blocking CP-AMPARs with IEM (100 μM) pretreatment (Fig. 9*L–O*).

We tested whether other ion channels contributed to Ca^{2+} accumulation in afferent terminals. To test whether voltage-

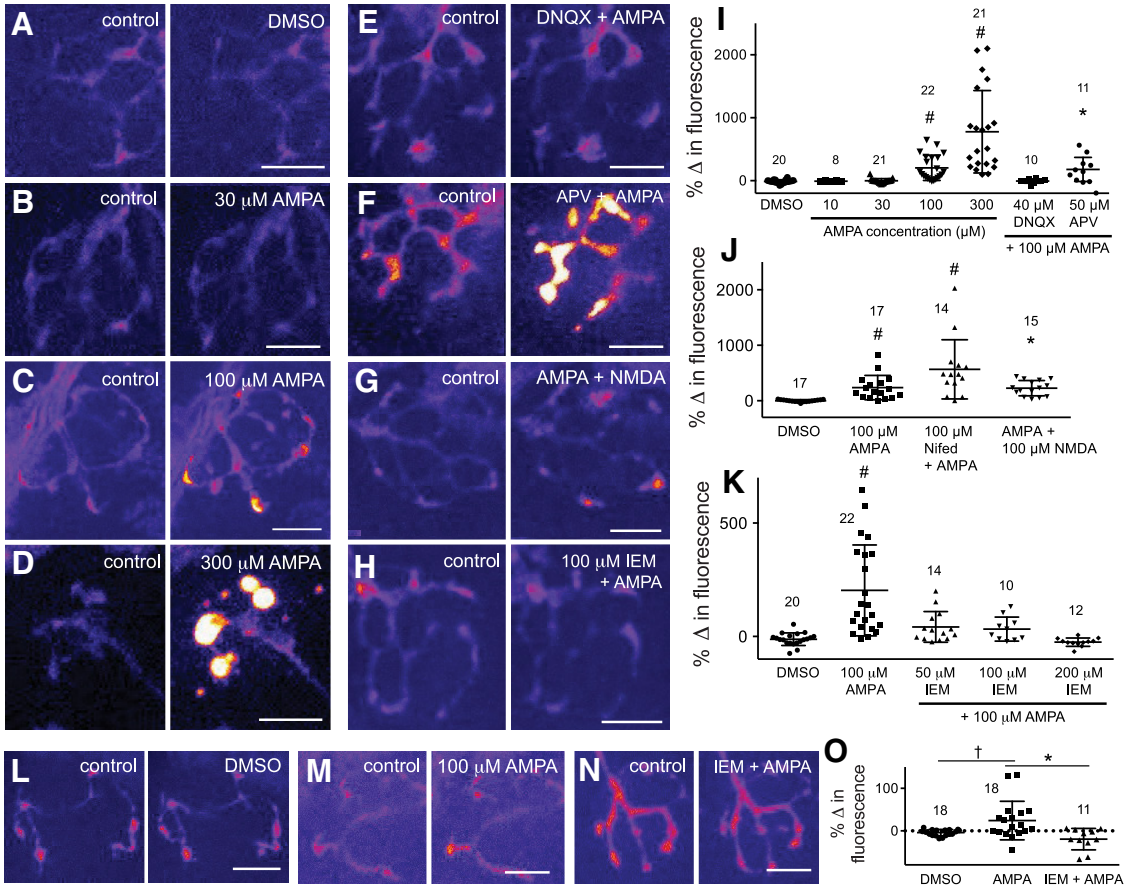

Figure 9. ***A–O***, High levels of AMPA cause an accumulation of terminal Ca^{2+} that is primarily mediated by Ca^{2+}-permeable AMPARs. *Tg[elavl3:GCaMP5G]* transgenics (***A–K***) and fish transiently expressing GCaMP3 in pLLG neurons [*hsp70l:GCaMP3–2.0cntnap2a*] (***L–O***) were used to measure intracellular Ca^{2+} levels in afferent terminals. ***A–H***, Maximum projections of afferent terminals in the untreated condition (control) and following AMPA application alone or application of a receptor antagonist followed by 100 μM AMPA. ***I***, AMPA has a dose-dependent effect on the accumulation of terminal Ca^{2+}. For all data points, the fluorescence intensity of a single terminal was measured in the untreated control condition and following drug application. The 100 and 300 μM concentrations of AMPA significantly increase the fluorescence intensity of terminals. This increase is blocked by DNQX and IEM, but not by the NMDAR blocker APV. ***J***, ***K***, Summary data showing the percentage change in terminal fluorescence intensity relative to the untreated control condition. ***K***, IEM suppresses the accumulation of terminal Ca^{2+} at all doses tested. ***L***, ***M***, Maximum projections of afferent terminals in the untreated condition (control) and following DMSO, AMPA application alone or application of a IEM followed by 100 μM AMPA. ***O***, Summary data showing that AMPA causes significant increases in fluorescence intensity that are blocked by IEM. Scale bars, 10 μm. One-way ANOVA: †$p < 0.05$; *$p < 0.01$; **$p < 0.001$; #$p < 0.0001$. *N* values are indicated in all plots above the data points.

gated Na^+ and K^+ channels are a requirement for Ca^{2+} accumulation, we anesthetized fish via bath application of the anesthetic tricaine. We found that Ca^{2+} accumulation was unchanged by tricaine. Moreover, AMPA had the same effects on GCaMP fluorescence regardless of whether fish were paralyzed with α-bungarotoxin or anesthetized with tricaine (Fig. 9*J*; two-way ANOVA). Pretreatment with nifedipine, an L-type voltage-gated Ca^{2+} channel blocker, did not block Ca^{2+} accumulation; rather, it somewhat enhanced AMPA-mediated Ca^{2+} accumulation relative to AMPA alone. We also tested for the presence of NMDAR-mediated Ca^{2+} entry using a zero Mg^{2+} solution. When we applied 100 μM NMDA after depolarizing terminals by bath application of 100 μM AMPA, we saw no further increase in GCaMP fluorescence over AMPA alone (Fig. 9*J*). As we were able to see an additional increase in fluorescence over treatment with 300 μM AMPA when compared with 100 μM AMPA, the GCaMP reporter should have been able to detect any additional effect of NMDA. We also compared GCaMP levels between the control condition and following application of one of the receptor blockers. At all DNQX, IEM, and APV doses tested, the antagonist alone had no effect on terminal fluorescence (percentage change relative to control − DNQX (40 μM), -5 ± 3, $n = 14$; APV (50 μM), 7 ± 12, $n = 14$; IEM (50 μM), -5 ± 3, $n = 14$; IEM (100 μM), -11 ± 2, $n = 10$; IEM (200 μM), -13 ± 4, $n = 12$; n = number of terminals). Together, these results suggest that a major source of terminal Ca^{2+} entry is through CP-AMPARs.

GluA2-lacking AMPARs reside at peripheral auditory synapses

To determine whether CP-AMPARs are found within the mature mammalian cochlea, we undertook quantitative analysis of the relative abundance of AMPAR subunits. Each mature mammalian auditory nerve fiber receives synaptic input from an inner hair cell via a single ribbon-type synapse with a single postsynaptic density, each expressing the Ca^{2+}-limiting AMPAR subunit GluA2 (Jing et al., 2013; Rutherford, 2015; Liberman and Liberman, 2016). Here, we show that these postsynaptic densities all coexpress GluA3 and GluA4 with GluA2 (Fig. 10). The total volume of AMPAR immunofluorescence was calculated for each synapse by thresholding a virtual channel created by summing the three individual confocal channels (GluA2, GluA3, and GluA4). Total AMPAR volume ranged from 0.09 to 0.85 μm^3/synapse. We calculated the intensity of each channel by summing the pixel values within each synaptic volume. Intensity of AMPAR sub-

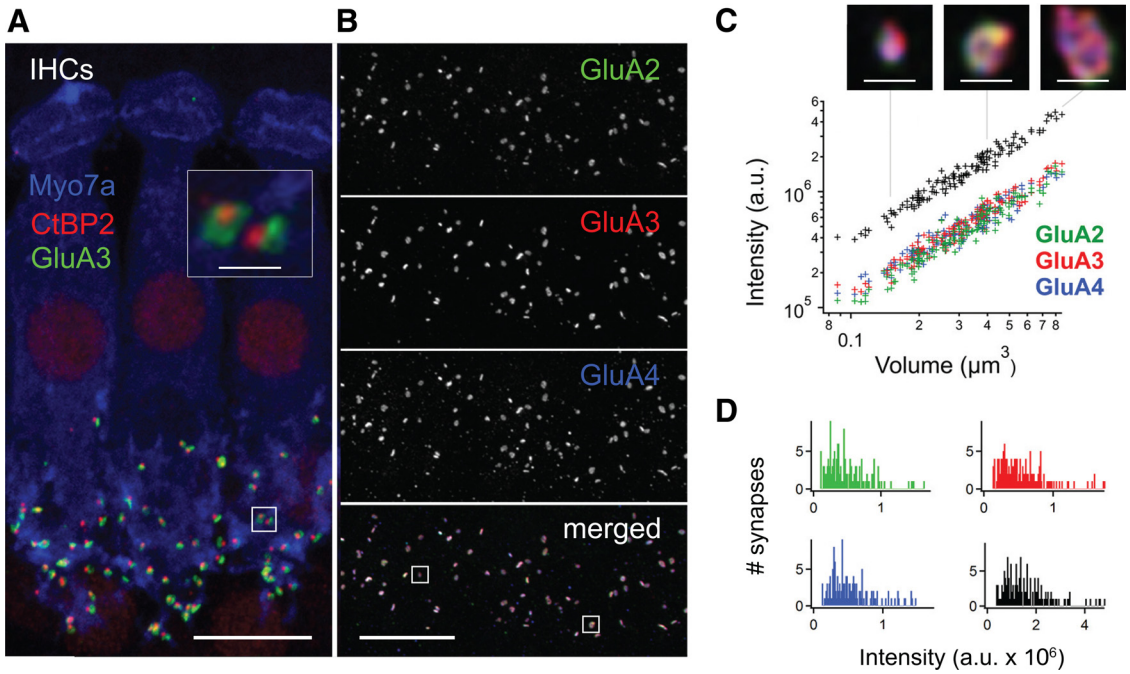

Figure 10. Postsynaptic densities of rat SGNs express the AMPAR subunits GluA2, GluA3, and GluA4. ***A***, Midcochlear region of the organ of Corti of a p25 rat immunolabeled with antibodies to GluA2 (green), GluA3 (red), and GluA4 (blue), imaged with confocal microscopy in the excised whole-mount preparation, shown in merged color and in grayscale. All synapses expressed each of the three AMPAR subunits. ***B***, Immunofluorescence intensity per synapse for each AMPAR subunit scaled approximately linearly with overall volume of $GluA_{Sum}$. Intensities and volumes ranged in value over approximately one order of magnitude among synapses ($n = 147$ from ***A***). Acquisition parameters were adjusted to normalize signals to the maximum pixel intensity in the image on each channel, resulting in synapses with similar intensities on the three channels. ***C***, Frequency distributions of intensity per synapse were positively skewed with similar coefficients of variation: GluA2, 0.60; GluA3, 0.60; GluA4, 0.56; $GluA_{Sum}$, 0.58.

unit immunofluorescence per synapse scaled with volume over approximately one order of magnitude for GluA2, GluA3, GluA4, and their sum ($GluA_{Sum}$; Fig. 10*B*), suggesting differences among synapses in overall AMPAR abundance.

Although each postsynaptic density expressed all three GluA subunits, we found heterogeneity suggesting that different types of AMPAR channels were present. Differences in fluorescence ratios generated the appearance of synapses with different hues in merged color panels (Figs. 10*A*, 11*A*,*C*). At some synapses, GluA2, GluA3, and GluA4 appeared to occupy very similar overlapping regions. Within other synapses, the subunits appeared to occupy partially nonoverlapping domains. Analysis with line profiles revealed some GluA2-lacking regions within synapses (Fig. 11*B*, arrowheads). To represent the subunit heterogeneity across synapses, we calculated fluorescence intensity ratios for each subunit compared with the sum intensities of all subunits at each synapse. While fluorescence ratios do not measure relative subunit abundance at a given synapse (see Materials and Methods), comparisons of these ratios among all synapses provide a measure of the heterogeneity of subunit relative abundance. Although the mean fluorescence ratios were similar for the population of synapses (0.31, 0.35, and 0.34, respectively, for GluA2, GluA3, and GluA4), the distributions of fluorescence ratios per synapse revealed that GluA2, GluA3, and GluA4 were expressed in different ratios at different postsynaptic densities (Fig. 11*D*). GluA4 exhibited the largest range of fluorescence ratios among synapses, from 0.23 to 0.47. In summary, the distribution of AMPAR subunits within and among synapses appears to be heterogeneous and is consistent with the presence of subregions with some GluA2 lacking CP-AMPARs, even though all synapses contain GluA2 subunits.

Calcium-permeable AMPARs mediate synaptic currents at an adult auditory synapse

Our studies in fish and rats have demonstrated that CP-AMPARs mediate excitotoxic damage and may be expressed in mature mammalian hair cell synapses. However, to determine whether synaptically released glutamate can activate CP-AMPARs *in vitro*, paired recordings between single hair cells and their afferent fibers are necessary. However, this has proven to be extremely difficult in mature mammalian cochlea. We thus performed paired recordings between auditory hair cells and their afferent fibers in adult bullfrog amphibian papilla, an organ that detects airborne sounds of low frequency (100–1200 Hz; Smotherman and Narins, 2000; Li et al., 2014). Figure 12*A* shows an example recording of a hair cell and afferent fiber together with simultaneous time-resolved membrane capacitance measurements (a presynaptic measure of synaptic vesicle exocytosis; Li et al., 2009). The voltage-clamped hair cell was depolarized from −90 to −30 mV for 20 ms. This elicits a calcium current (I_{Ca}) and a C_m jump from the hair cell, and an EPSC in the afferent fiber (black trace). At this synapse, the EPSC charge is well correlated to the C_m jump (Cho et al., 2011). The EPSC is mediated by the opening of AMPA receptors in the afferent fiber (Keen and Hudspeth, 2006). It is composed of an initial phasic component followed by a tonic sustained component. This EPSC was partly blocked by 60 μM IEM, a use-dependent-specific open channel blocker of CP-AMPARs (Kim and von Gersdorff, 2016). Note that the large phasic peak of the EPSC was completely blocked after 7 min and 20 s in IEM, whereas the size of the C_m jump did not change (Fig. 12*A*).

The EPSC block by IEM was use dependent and progressive. Figure 12*B* shows the progressive block of the EPSCs in the continuous presence of IEM by successive 20 ms depolarizing pulses

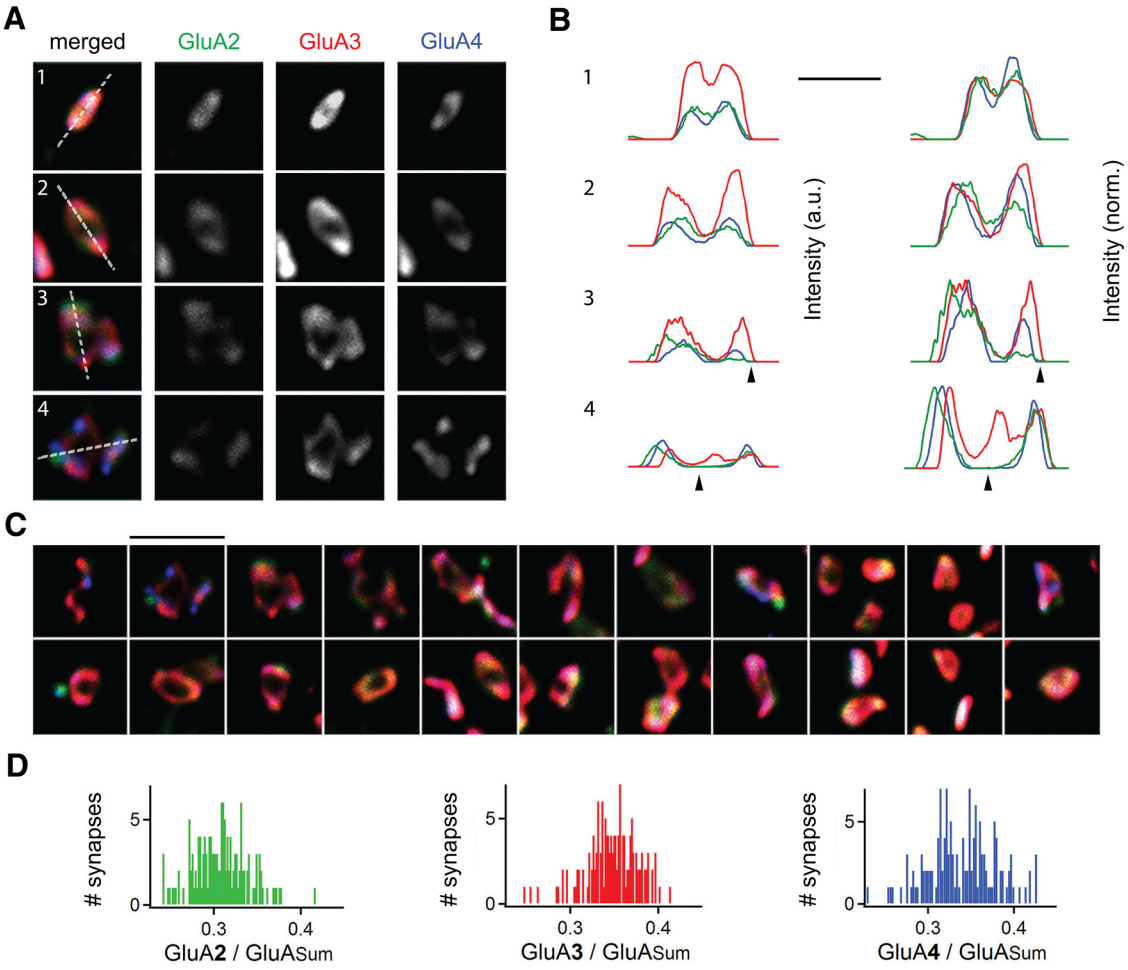

Figure 11. AMPAR subunits appear to occupy partially nonoverlapping domains, suggesting the existence of GluA2-lacking receptor channels in some postsynaptic densities in a mammalian cochlea. ***A***, Confocal immunofluorescence for the three AMPAR subunits, on p25 rat postsynaptic densities oriented en face, shown separately in grayscale and merged in color. GluA2 (green), GluA3 (red), and GluA4 (blue) appear to occupy similar regions in examples 1 and 2. In examples 3 and 4, the subunits appear to reside in partially nonoverlapping domains. ***B***, Line profiles of fluorescence intensity for the four synapses, as shown on the merged color images in ***A***. The mean pixel intensity (*y*-axis, in arbitrary units) over a 120-nm-wide band perpendicular to the line was plotted as a function of distance along the line (*x*-axis, in micrometers). On the left, line profiles are shown in absolute scale to illustrate differences between synapses in the same acquired image volume. On the right, line profiles have been normalized to the maximum amplitude of the first peaks in each plot to highlight spatial differences in GluA composition within synapses. Line profiles across postsynaptic densities 3 and 4 suggest the existence of GluA2-lacking regions (arrowheads). ***C***, Images of postsynaptic densities oriented en face with subunit immunoreactivities colored as in ***A***. The subunits appear to occupy partially nonoverlapping domains in some synapses but not in others. ***D***, Frequency distributions of intensity ratios ($GluA_{subunit}/GluA_{Sum}$) compare a representative population of synapses from one image volume (shown in Fig. 1*A*), where synapses all having identical relative subunit compositions would exhibit ratios of 0.33 for each GluA subunit. Instead, fractional fluorescence ranged from ~0.25 to 0.4 for GluA2 (left), GluA3 (center), and GluA4 (right). Scale bars: ***B***, 1 μm; ***C***, 2 μm.

to the hair cell. The low affinity for glutamate of AMPARs, and perhaps the heterogeneous release probability of the synapse, may require repeated bouts of multiquantal glutamate release to produce complete block of EPSCs mediated by CP-AMPAR. Figure 12*C* shows that 60 μM IEM reduced significantly the total charge of the EPSCs. After 5 min of IEM application, the average charge of EPSCs was decreased by 31.5 ± 4.2% (n = 16 pairs). Among these 16 pairs, 5 pairs showed smaller effects on the decrease of EPSC charges (13.0 ± 3.4%). After 8 min of IEM application, the average charge of the EPSCs was further decreased by 39.3 ± 6.0% (n = 8 pairs) without significant changes in the membrane capacitance jump. Because the large and phasic EPSC is responsible for rapid spike triggering in the afferent fibers (Schnee et al., 2013; Graydon et al., 2014), we also analyzed the amount of IEM block in the first 5 ms after the depolarizing pulse to the hair cell. During the first 5 ms, IEM decreased the EPSC charge by 44.9 ± 8.7%. These data clearly demonstrated that CP-AMPARs comprise a substantial component of the glutamatergic transmission at this mature auditory ribbon-type synapse.

Discussion

Using *in vivo* electrophysiology and Ca^{2+} imaging, we demonstrate that CP-AMPARs mediate glutamatergic transmission and excitotoxic damage at synapses between hair cells and their afferent neurons. Our study extends previous findings in acoustic-lateralis endorgans by demonstrating that CP-AMPARs mediate a major component of the afferent terminal synaptic response in adult auditory synapses of the frog. We demonstrate that excitotoxic damage of lateral line synapses in the zebrafish is associated with Ca^{2+} accumulation and that those synapses can be protected by pharmacological blockade of CP-AMPARs. Moreover, simultaneous immunohistochemistry for GluA2, GluA3, and GluA4 at mature afferent synapses in the mammalian cochlea suggests the existence of AMPA receptors lacking the Ca^{2+}-limiting GluA2 subunit. Together, these findings suggest that CP-AMPARs are a common feature of primary afferent synapses in vertebrate acoustic-lateralis endorgans.

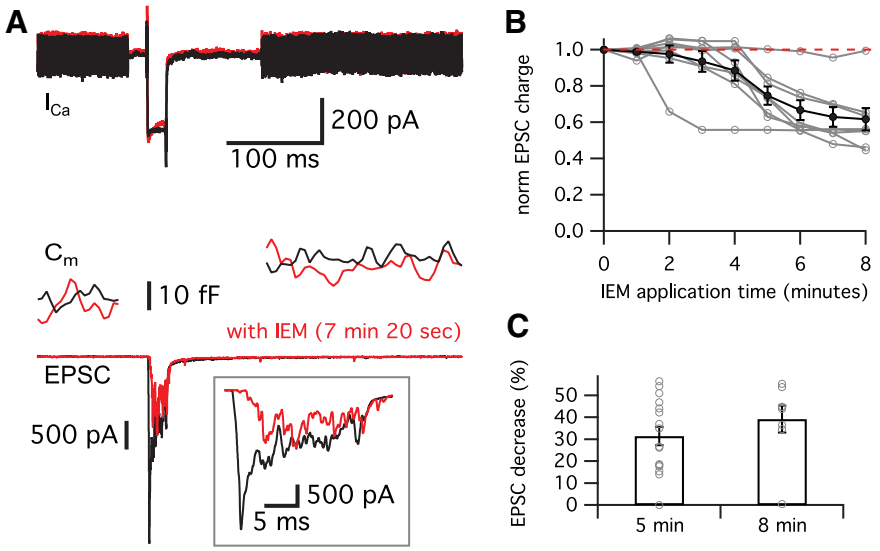

Figure 12. CP-AMPARs mediate a substantial component of the synaptic transmission at auditory hair cell synapses in adult bullfrogs. ***A***, Representative trace of paired whole-cell voltage-clamp recordings of an amphibian papilla hair cell and a postsynaptic afferent fiber, with simultaneous C_m measurements from the hair cell, which was depolarized from −90 to −30 mV for 20 ms. This depolarization elicits an I_{Ca} in the hair cell that triggers a C_m change produced by the exocytosis of synaptic vesicles. The traces are recorded before (control, black) and after applying 60 μM IEM (at 7 min 20 s after IEM application, red). The inset shows that the initial phasic EPSC was dramatically reduced by IEM. ***B***, The normalized charges of EPSCs are shown as a function of time since the IEM application. The average of normalized EPSC charges are shown in black at each time point, and individual data points are shown in gray ($n = 8$ pairs). The red dashed line indicates a value of 1. In the continuous presence of IEM, the EPSC charge is progressively blocked by successive 20 ms depolarizing pulses to the hair cell. ***C***, The application of 60 μM IEM reduced the charge of the EPSCs. After 5 min of IEM application, the average charge of the EPSCs was decreased by 31.5 ± 4.2% ($n = 16$ pairs) compared with control. After 8 min of IEM application, the average charge of the EPSCs was further decreased by 39.3 ± 6.0% ($n = 8$ pairs).

Presynaptic versus postsynaptic mechanisms of excitotoxic damage in the lateral line

Our findings with immunohistochemical (Fig. 8) and Ca^{2+} imaging experiments (Fig. 4) suggest that the loss of terminal responsiveness following AMPA exposure is due to a loss of postsynaptic sensitivity instead of a restructuring of the synapse. Immunohistochemistry suggested that, despite substantial terminal swelling, the presynaptic and postsynaptic components remained intact at many synapses (Fig. 8). Yet it remains possible that the loss of postsynaptic terminal responsiveness following AMPA exposure was due to hair cell damage affecting presynaptic glutamate release (Sheets, 2017). Our current studies do not thoroughly address this possibility. However, lateral line hair cell responses to mechanical stimulation were intact after AMPA application (Fig. 5). This was assayed by water jet-evoked intracellular Ca^{2+} signals in hair cells, which are a measure of mechanotransduction and presumably a depolarized receptor potential (Kindt et al., 2012). The extent to which the loss of postsynaptic terminal responses resulted from the loss of presynaptic release from the stimulated hair cell, versus loss of postsynaptic sensitivity of the afferent fiber, remains to be explored.

Ca^{2+}-permeable AMPARs at auditory hair cell afferent synapses in the amphibian papilla

In addition to showing that CP-AMPARs contribute to AMPA-mediated Ca^{2+} influx in the fish, we have demonstrated that CP-AMPARs mediate a major component of glutamatergic transmission in auditory hair cell synapses of the bullfrog. Our finding that IEM1460 reduced the synaptic current charge by ~40% suggests that a large portion of the EPSC in the amphibian papilla is carried by CP-AMPARs (Fig. 12). In addition to Ca^{2+} permeability, the GluA2 subunit has been shown in other systems to influence several properties of AMPARs including EPSC kinetics (Geiger et al., 1995; Washburn et al., 1997). For example, AMPARs in the avian cochlear nucleus have high Ca^{2+} permeability and fast kinetics (Otis et al., 1995). EPSCs at hair cell afferent synapses have large amplitudes and submillisecond rise and decay kinetics (Glowatzki and Fuchs, 2002; Keen and Hudspeth, 2006), which are properties that promote spike phase locking to sound frequency (Li et al., 2014; Heil and Peterson, 2017). In addition to reducing the overall EPSC charge, IEM1460 greatly reduced and delayed the peak of the EPSC (Fig. 12*A*, inset). The initial phasic EPSC is thus mediated mostly by the opening of CP-AMPARs after synaptically released glutamate. As expected for a use-dependent open channel blocker of CP-AMPARs, this reduction by IEM1460 was activity dependent (Fig. 12*B*). It remains to be seen whether CP-AMPARs carry a significant fraction of the EPSC in terminals of auditory nerve fibers in the mammalian cochlea, which are postsynaptic to inner hair cell synaptic ribbons.

GluA2-lacking AMPARs at hair cell synapses in the mammalian cochlea

Cochlear hair cell afferent synapses contain postsynaptic AMPARs including the Ca^{2+}-limiting GluA2 subunit (Fig. 11). Expression of the GluA2 subunit juxtaposed to the presynaptic ribbon is used to define a synapse, and count them, over development and in response to acoustic trauma (Liberman et al., 2015; Liberman and Liberman, 2016). The presence of GluA2 at all synapses has contributed to the general assumption that AMPARs in the mammalian cochlea are relatively impermeable to Ca^{2+}.

AMPA-stimulated Ca^{2+} entry into postsynaptic terminals has been proposed as the cause of excitotoxic damage to auditory nerve fibers, primarily because Ca^{2+} influx through glutamate receptors is a well studied excitotoxic mechanism in the brain (Sattler and Tymianski, 2001). However, its relevance in the inner ear is unclear. Cobalt staining, used as a proxy for Ca^{2+} entry (Pruss et al., 1991), has suggested that AMPA induces Ca^{2+} entry into SGNs (Eybalin et al., 2004). However, given that kainate receptors, NMDA receptors, and voltage-gated Ca^{2+} channels may mediate Ca^{2+} influx as well, it is still unclear whether CP-AMPARs are directly involved in cochlear excitotoxicity.

Acoustic overstimulation results in swelling of auditory nerve fiber terminals on hair cells, which express GluA2, GluA3, and GluA4 (Fig. 10). With confocal microscopy, we found GluA2-lacking regions within postsynaptic densities of some auditory nerve fiber terminals in the rat (Fig. 11). This suggests that, although all postsynaptic densities expressed GluA-2, some of the AMPAR tetramers may lack the GluA2 subunit. On most postsynaptic densities, the three AMPAR subunits appeared to overlap each other at confocal resolution. Future work with super-resolution light microscopy is needed to assess the prevalence of GluA2-lacking regions within synapses. At central synapses including those in the calyx of Held in the mouse auditory brainstem, the presence of GluA4 in GluA3/4-containing AMPARs is indispensable for driving fast neu-

rotransmission (Yang et al., 2011). The existence of functional GluA2-lacking CP-AMPARs and their role in cochlear synaptic transmission remains to be tested. At hair cell synapses, relatively fast kinetics and Ca^{2+} permeability of GluA2-lacking AMPARs may be important for fast auditory signaling during phase locking as well as for understanding mechanisms of excitotoxicity upon overexposure to sound.

References

Ahrens MB, Orger MB, Robson DN, Li JM, Keller PJ (2013) Whole-brain functional imaging at cellular resolution using light-sheet microscopy. Nat Methods 10:413–420. CrossRef Medline

Chang JL, Brauer DS, Johnson J, Chen CG, Akil O, Balooch G, Humphrey MB, Chin EN, Porter AE, Butcher K, Ritchie RO, Schneider RA, Lalwani A, Derynck R, Marshall GW, Marshall SJ, Lustig L, Alliston T (2010) Tissue-specific calibration of extracellular matrix material properties by transforming growth factor-beta and Runx2 in bone is required for hearing. EMBO Rep 11:765–771. CrossRef Medline

Cho S, Li GL, von Gersdorff H (2011) Recovery from short-term depression and facilitation is ultrafast and Ca^{2+} dependent at auditory hair cell synapses. J Neurosci 31:5682–5692. CrossRef Medline

Esterberg R, Hailey DW, Coffin AB, Raible DW, Rubel EW (2013) Disruption of intracellular calcium regulation is integral to aminoglycoside-induced hair cell death. J Neurosci 33:7513–7525. CrossRef Medline

Eybalin M, Caicedo A, Renard N, Ruel J, Puel JL (2004) Transient Ca^{2+}-permeable AMPA receptors in postnatal rat primary auditory neurons. Eur J Neurosci 20:2981–2989. CrossRef Medline

Fujikawa T, Petralia RS, Fitzgerald TS, Wang YX, Millis B, Morgado-Díaz JA, Kitamura K, Kachar B (2014) Localization of kainate receptors in inner and outer hair cell synapses. Hear Res 314:20–32. CrossRef Medline

Geiger JR, Melcher T, Koh DS, Sakmann B, Seeburg PH, Jonas P, Monyer H (1995) Relative abundance of subunit mRNAs determines gating and Ca^{2+} permeability of AMPA receptors in principal neurons and interneurons in rat CNS. Neuron 15:193–204. CrossRef Medline

Gillis KD (2000) Admittance-based measurement of membrane capacitance using the EPC-9 patch-clamp amplifier. Pflugers Arch 439:655–664. CrossRef Medline

Glowatzki E, Fuchs PA (2002) Transmitter release at the hair cell ribbon synapse. Nat Neurosci 5:147–154. CrossRef Medline

Goutman JD, Glowatzki E (2007) Time course and calcium dependence of transmitter release at a single ribbon synapse. Proc Natl Acad Sci U S A 104:16341–16346. CrossRef Medline

Graydon CW, Cho S, Diamond JS, Kachar B, von Gersdorff H, Grimes WN (2014) Specialized postsynaptic morphology enhances neurotransmitter dilution and high-frequency signaling at an auditory synapse. J Neurosci 34:8358–8372. CrossRef Medline

Heil P, Peterson AJ (2017) Spike timing in auditory-nerve fibers during spontaneous activity and phase locking. Synapse 71:5–36. CrossRef Medline

Higashijima S, Hotta Y, Okamoto H (2000) Visualization of cranial motor neurons in live transgenic zebrafish expressing green fluorescent protein under the control of the islet-1 promoter/enhancer. J Neurosci 20:206–218. Medline

Hoppmann V, Wu JJ, Soviknes AM, Helvik JV, Becker TS (2008) Expression of the eight AMPA receptor subunit genes in the developing central nervous system and sensory organs of zebrafish. Dev Dyn 237:788–799. CrossRef Medline

Jia Z, Agopyan N, Miu P, Xiong Z, Henderson J, Gerlai R, Taverna FA, Velumian A, MacDonald J, Carlen P, Abramow-Newerly W, Roder J (1996) Enhanced LTP in mice deficient in the AMPA receptor GluR2. Neuron 17:945–956. CrossRef Medline

Jing Z, Rutherford MA, Takago H, Frank T, Fejtova A, Khimich D, Moser T, Strenzke N (2013) Disruption of the presynaptic cytomatrix protein bassoon degrades ribbon anchorage, multiquantal release, and sound encoding at the hair cell afferent synapse. J Neurosci 33:4456–4467. CrossRef Medline

Jonas P, Burnashev N (1995) Molecular mechanisms controlling calcium entry through AMPA-type glutamate receptor channels. Neuron 15:987–990. CrossRef Medline

Keen EC, Hudspeth AJ (2006) Transfer characteristics of the hair cell's afferent synapse. Proc Natl Acad Sci U S A 103:5537–5542. CrossRef Medline

Kim KX, Rutherford MA (2016) Maturation of NaV and KV channel topographies in the auditory nerve spike initiator before and after developmental onset of hearing function. J Neurosci 36:2111–2118. CrossRef Medline

Kim MH, von Gersdorff H (2016) Postsynaptic plasticity triggered by Ca^{2+}-permeable AMPA receptor activation in retinal amacrine cells. Neuron 89:507–520. CrossRef Medline

Kindt KS, Finch G, Nicolson T (2012) Kinocilia mediate mechanosensitivity in developing zebrafish hair cells. Dev Cell 23:329–341. CrossRef Medline

Kujawa SG, Liberman MC (2009) Adding insult to injury: cochlear nerve degeneration after "temporary" noise-induced hearing loss. J Neurosci 29:14077–14085. CrossRef Medline

Kuriyama H, Jenkins O, Altschuler RA (1994) Immunocytochemical localization of AMPA selective glutamate-receptor subunits in the rat cochlea. Hear Res 80:233–240. CrossRef Medline

Lau A, Tymianski M (2010) Glutamate receptors, neurotoxicity and neurodegeneration. Pflugers Arch 460:525–542. CrossRef Medline

Li GL, Keen E, Andor-Ardó D, Hudspeth AJ, von Gersdorff H (2009) The unitary event underlying multiquantal EPSCs at a hair cell's ribbon synapse. J Neurosci 29:7558–7568. CrossRef Medline

Li GL, Cho S, von Gersdorff H (2014) Phase-locking precision is enhanced by multiquantal release at an auditory hair cell ribbon synapse. Neuron 83:1404–1417. CrossRef Medline

Liberman LD, Liberman MC (2016) Postnatal maturation of auditory-nerve heterogeneity, as seen in spatial gradients of synapse morphology in the inner hair cell area. Hear Res 339:12–22. CrossRef Medline

Liberman LD, Suzuki J, Liberman MC (2015) Dynamics of cochlear synaptopathy after acoustic overexposure. J Assoc Res Otolaryngol 16:205–219. CrossRef Medline

Lin HW, Furman AC, Kujawa SG, Liberman MC (2011) Primary neural degeneration in the Guinea pig cochlea after reversible noise-induced threshold shift. J Assoc Res Otolaryngol 12:605–616. CrossRef Medline

Lindau M, Neher E (1988) Patch-clamp techniques for time-resolved capacitance measurements in single cells. Pflugers Arch 411:137–146. CrossRef Medline

Liu SJ, Zukin RS (2007) Ca2+-permeable AMPA receptors in synaptic plasticity and neuronal death. Trends Neurosci 30:126–134. CrossRef Medline

Lv C, Stewart WJ, Akanyeti O, Frederick C, Zhu J, Santos-Sacchi J, Sheets L, Liao JC, Zenisek D (2016) Synaptic ribbons require ribeye for electron density, proper synaptic localization, and recruitment of calcium channels. Cell Rep 15:2784–2795. CrossRef Medline

Maeda R, Kindt KS, Mo W, Morgan CP, Erickson T, Zhao H, Clemens-Grisham R, Barr-Gillespie PG, Nicolson T (2014) Tip-link protein protocadherin 15 interacts with transmembrane channel-like proteins TMC1 and TMC2. Proc Natl Acad Sci U S A 111:12907–12912. CrossRef Medline

Matsubara A, Laake JH, Davanger S, Usami S, Ottersen OP (1996) Organization of AMPA receptor subunits at a glutamate synapse: a quantitative Immunogold analysis of hair cell synapses in the rat organ of Corti. J Neurosci 16:4457–4467. Medline

Medvedev NI, Rodríguez-Arellano JJ, Popov VI, Davies HA, Tigaret CM, Schoepfer R, Stewart MG (2008) The glutamate receptor 2 subunit controls post-synaptic density complexity and spine shape in the dentate gyrus. Eur J Neurosci 27:315–325. CrossRef Medline

Nicolson T (2005) The genetics of hearing and balance in zebrafish. Annu Rev Genet 39:9–22. CrossRef Medline

Obholzer N, Wolfson S, Trapani JG, Mo W, Nechiporuk A, Busch-Nentwich E, Seiler C, Sidi S, Söllner C, Duncan RN, Boehland A, Nicolson T (2008) Vesicular glutamate transporter 3 is required for synaptic transmission in zebrafish hair cells. J Neurosci 28:2110–2118. CrossRef Medline

Ohn TL, Rutherford MA, Jing Z, Jung S, Duque-Afonso CJ, Hoch G, Picher MM, Scharinger A, Strenzke N, Moser T (2016) Hair cells use active zones with different voltage dependence of Ca^{2+} influx to decompose sounds into complementary neural codes. Proc Natl Acad Sci U S A 113:E4716–E4725. CrossRef Medline

Otis TS, Raman IM, Trussell LO (1995) AMPA receptors with high Ca^{2+} permeability mediate synaptic transmission in the avian auditory pathway. J Physiol 482:309–315. CrossRef Medline

Pruss RM, Akeson RL, Racke MM, Wilburn JL (1991) Agonist-activated cobalt uptake identifies divalent cation-permeable kainate receptors on neurons and glial cells. Neuron 7:509–518. CrossRef Medline

Puel JL, Pujol R, Ladrech S, Eybalin M (1991) Alpha-amino-3-hydroxy-5-

methyl-4-isoxazole propionic acid electrophysiological and neurotoxic effects in the guinea-pig cochlea. Neuroscience 45:63–72. CrossRef Medline

Puel JL, Pujol R, Tribillac F, Ladrech S, Eybalin M (1994) Excitatory amino acid antagonists protect cochlear auditory neurons from excitotoxicity. J Comp Neurol 341:241–256. CrossRef Medline

Puel JL, Ruel J, Gervais d'Aldin C, Pujol R (1998) Excitotoxicity and repair of cochlear synapses after noise-trauma induced hearing loss. Neuroreport 9:2109–2114. CrossRef Medline

Pujol-Marti J, Zecca A, Baudoin JP, Faucherre A, Asakawa K, Kawakami K, Lopez-Schier H (2012) Neuronal birth order identifies a dimorphic sensorineural map. J Neurosci 32:2976–2987. CrossRef Medline

Puller C, Haverkamp S (2011) Bipolar cell pathways for color vision in non-primate dichromats. Vis Neurosci 28:51–60. CrossRef Medline

Puthussery T, Percival KA, Venkataramani S, Gayet-Primo J, Grünert U, Taylor WR (2014) Kainate receptors mediate synaptic input to transient and sustained OFF visual pathways in primate retina. J Neurosci 34:7611–7621. CrossRef Medline

Rutherford MA (2015) Resolving the structure of inner ear ribbon synapses with STED microscopy. Synapse 69:242–255. CrossRef Medline

Sagata N, Iwaki A, Aramaki T, Takao K, Kura S, Tsuzuki T, Kawakami R, Ito I, Kitamura T, Sugiyama H, Miyakawa T, Fukumaki Y (2010) Comprehensive behavioural study of GluR4 knockout mice: implication in cognitive function. Genes Brain Behav 9:899–909. CrossRef Medline

Sattler R, Tymianski M (2001) Molecular mechanisms of glutamate receptor-mediated excitotoxic neuronal cell death. Mol Neurobiol 24:107–129. CrossRef Medline

Schnee ME, Castellano-Muñoz M, Ricci AJ (2013) Response properties from turtle auditory hair cell afferent fibers suggest spike generation is driven by synchronized release both between and within synapses. J Neurophysiol 110:204–220. CrossRef Medline

Sheets L, Trapani JG, Mo W, Obholzer N, Nicolson T (2011) Ribeye is required for presynaptic Ca(V)1.3a channel localization and afferent innervation of sensory hair cells. Development 138:1309–1319. CrossRef Medline

Sheets L (2017) Excessive activation of ionotropic glutamate receptors induces apoptotic hair-cell death independent of afferent and efferent innervation. Sci Rep 7:41102. CrossRef Medline

Smotherman MS, Narins PM (2000) Hair cells, hearing and hopping: a field guide to hair cell physiology in the frog. J Exp Biol 203:2237–2246. Medline

Söllner C, Rauch GJ, Siemens J, Geisler R, Schuster SC, Müller U, Nicolson T, Tübingen Screen C (2004) Mutations in cadherin 23 affect tip links in zebrafish sensory hair cells. Nature 428:955–959. CrossRef Medline

Stewart WJ, Cardenas GS, McHenry MJ (2013) Zebrafish larvae evade predators by sensing water flow. J Exp Biol 216:388–398. CrossRef Medline

Suli A, Watson GM, Rubel EW, Raible DW (2012) Rheotaxis in larval zebrafish is mediated by lateral line mechanosensory hair cells. PLoS One 7:e29727. CrossRef Medline

Trapani JG, Nicolson T (2010) Physiological recordings from zebrafish lateral-line hair cells and afferent neurons. Methods Cell Biol 100:219–231. CrossRef Medline

Trapani JG, Nicolson T (2011) Mechanism of spontaneous activity in afferent neurons of the zebrafish lateral-line organ. J Neurosci 31:1614–1623. CrossRef Medline

Trussell LO, Zhang S, Raman IM (1993) Desensitization of AMPA receptors upon multiquantal neurotransmitter release. Neuron 10:1185–1196. CrossRef Medline

Vissavajjhala P, Janssen WG, Hu Y, Gazzaley AH, Moran T, Hof PR, Morrison JH (1996) Synaptic distribution of the AMPA-GluR2 subunit and its colocalization with calcium-binding proteins in rat cerebral cortex: an immunohistochemical study using a GluR2-specific monoclonal antibody. Exp Neurol 142:296–312. CrossRef Medline

Wang J, Zhang B, Jiang H, Zhang L, Liu D, Xiao X, Ma H, Luo X, Bojrab D 2nd, Hu Z (2013) Myelination of the postnatal mouse cochlear nerve at the peripheral-central nervous system transitional zone. Front Pediatr 1:43. CrossRef Medline

Washburn MS, Numberger M, Zhang S, Dingledine R (1997) Differential dependence on GluR2 expression of three characteristic features of AMPA receptors. J Neurosci 17:9393–9406. Medline

Wenthold RJ, Yokotani N, Doi K, Wada K (1992) Immunochemical characterization of the non-NMDA glutamate receptor using subunit-specific antibodies. Evidence for a hetero-oligomeric structure in rat brain. J Biol Chem 267:501–507. Medline

Yang YM, Aitoubah J, Lauer AM, Nuriya M, Takamiya K, Jia Z, May BJ, Huganir RL, Wang LY (2011) GluA4 is indispensable for driving fast neurotransmission across a high-fidelity central synapse. J Physiol 589:4209–4227. CrossRef Medline

Zhang-Hooks Y, Agarwal A, Mishina M, Bergles DE (2016) NMDA receptors enhance spontaneous activity and promote neuronal survival in the developing cochlea. Neuron 89:337–350. CrossRef Medline